Title Page

Title: Inhibitory parvalbumin basket cells are selectively impaired during hippocampal sharp wave ripples in a mouse model of familial Alzheimer's disease

Abbrev Title: PVBCs are impaired during SWRs in model of AD

Authors: Adam Caccavano[1*], P. Lorenzo Bozzelli[1], Patrick A. Forcelli[1,2], Daniel T.S. Pak[1,2], Jian-Young Wu[1,3], Katherine Conant[1,3], Stefano Vicini[1,2]

Affiliations: [1]Interdisciplinary Program in Neuroscience, Georgetown University Medical Center, Washington, DC, 20057, [2]Dept. of Pharmacology & Physiology, Georgetown University Medical Center, Washington, DC, 20057, [3]Dept. of Neuroscience, Georgetown University Medical Center, Washington, DC, 20057, *Corresponding Author

Corresponding author email address: ac1625@georgetown.edu

Number of pages: 52

Number of figures, tables: 1 table, 8 figures

Number of words (abstract, significance statement, introduction, discussion): 246; 116; 597; 1500

Conflict of Interest Statement: The authors declare no competing financial interests.

Acknowledgements: AC was supported by NIH/NIA F31 AG062030, NIH/NCATS TL1 TR001431, and the ARCS Foundation. DP and SV were partially supported by NIH/NIA RF1 AG056603. KC and SV were partially supported by NIH/NINDS R01 NS108810. The content is solely the responsibility of the authors and does not necessarily represent the official views of the National Institutes of Health.

Abstract

Memory disruption in mild cognitive impairment (MCI) and Alzheimer's disease (AD) is poorly understood, particularly at early stages prior to neuronal or synaptic degeneration. In mouse models of AD, there are observed disruptions to sharp wave ripples (SWRs), hippocampal population events with a critical role in memory consolidation. However, the micro-circuitry underlying these disruptions are under-explored. We tested the hypothesis that a selective reduction in parvalbumin-expressing (PV) inhibitory interneuron activity underlies hyperactivity and SWR disruption. We employed the 5xFAD model of familial Alzheimer's disease crossed with mouse lines that selectively label excitatory pyramidal cells (PCs) and inhibitory PV cells. We observed a 33% increase in frequency, 58% increase in amplitude, and 8% decrease in duration of SWRs in acute slices from 3-month 5xFAD mice versus littermate controls. 5xFAD mice of the same age were impaired in a task of hippocampal-dependent memory. Concurrent with SWR recordings, we performed calcium imaging, cell-attached, and whole-cell recordings of PC and PV cells within the CA1 region. PCs in 5xFAD mice participated in enlarged ensembles, with similar spiking activity, and increased synaptic E/I ratio, suggesting a disinhibitory mechanism. In contrast, we observed a selective 46% spike rate reduction during SWRs in PV basket cells (PVBCs), whereas PV bistratified and PV axo-axonic cells were unimpaired. Excitatory synaptic drive to PVBCs was selectively reduced by 50%, resulting in decreased E/I ratio. Considering prior studies of intrinsic PV cell dysfunction in AD, these findings suggest synaptic and network mechanisms also play a prominent role.

20 **Significance Statement**

21 We demonstrate that a specific sub-type of inhibitory neuron, PV-expressing basket cells, are
22 selectively impaired in a model of Alzheimer's disease during activity critical for the consolidation of
23 memory (i.e. SWRs). These results identify a cellular target for therapeutic intervention to restore aberrant
24 network activity in early amyloid pathology. While PV-expressing cells have previously been identified as
25 a potential therapeutic target, this study for the first time recognizes that other PV-expressing neuronal
26 sub-types, including bistratified and axo-axonic cells, are spared. It also represents the first attempt to
27 record synaptic and spiking activity during SWR events in early amyloid pathology, revealing that a
28 selective decrease in excitatory synaptic drive to PV basket cells likely underlies reduced function.

Introduction

Alzheimer's disease (AD) is the leading cause of dementia, and a growing public health crisis as worldwide life expectancy increases (Mattson, 2004). AD is characterized by learning and memory deficits, the pathological accumulation of amyloid beta (Aβ) plaques and neurofibrillary tangles, and synaptic and neuronal degeneration (Serrano-Pozo et al., 2011). The cause of memory disruption in the disease is poorly understood, particularly at early ages prior to widespread neurodegeneration. The hippocampus, a region particularly important for the encoding and consolidation of spatial memory, is one of the first regions impaired in AD (Braak and Braak, 1991). Hyperactivity within the hippocampus is observed in mouse models of AD (Palop et al., 2007; Busche et al., 2008, 2012; Palop and Mucke, 2010), as well as in clinical populations, where seizures are an increasingly recognized co-morbidity of AD (Hauser et al., 1986; Amatniek et al., 2006; Palop and Mucke, 2009). While it is well appreciated that Aβ impairs the synaptic function of excitatory pyramidal cells (PCs) in later disease progression (Kamenetz et al., 2003; Shankar et al., 2008; Pozueta et al., 2013), there is growing evidence of early deficits to inhibitory GABAergic cells (Li et al., 2016), potentially explaining this shift to hyperactivity through disinhibition. In particular, several functional impairments are observed in inhibitory parvalbumin-expressing (PV) fast-spiking interneurons (Verret et al., 2012; Mahar et al., 2016; Yang et al., 2016; Hijazi et al., 2019). However, there are at least three unique PV cell sub-types within the CA1 region of hippocampus with varying anatomical connections and function (Varga et al., 2014), and the separate impact of AD pathology on these sub-types is unknown.

PV cells play a critical role in hippocampal sharp wave ripples (Ellender et al., 2010; Schlingloff et al., 2014; Ognjanovski et al., 2017), spontaneous neuronal population events characterized by a low frequency sharp wave (1-30 Hz) and a high frequency ripple (120-250 Hz) (Buzsáki, 1986, 2015; Colgin, 2016). SWRs principally originate in the CA3 region and propagate to CA1 along the Schaffer collaterals, occurring in all mammalian species studied to date (Buzsáki et al., 2013). Even following decortication in brain slices, SWRs spontaneously arise in hippocampus (Buzsáki et al., 1983). SWRs have been extensively studied in large part due to their proposed role in memory consolidation (Wilson and McNaughton, 1994; Kudrimoti et al., 1999; O'Neill et al., 2008; Karlsson and Frank, 2009). Sequences of

place cells activated during spatial learning replay in temporally compressed neuronal ensembles within SWRs during rest (Nádasdy et al., 1999; Lee and Wilson, 2002). Online interruption of SWRs through both electrical (Girardeau et al., 2009; Ego-Stengel and Wilson, 2010) and optogenetic stimulation (Ven et al., 2016; Roux et al., 2017) leads to learning and memory deficits, demonstrating their critical role in memory consolidation. Notably, in several mouse models of AD, SWRs are disrupted (Gillespie et al., 2016; Iaccarino et al., 2016; Nicole et al., 2016; Xiao et al., 2017; Hollnagel et al., 2019; Jones et al., 2019; Jura et al., 2019). However, the micro-circuitry underlying these disruptions has yet to be explored in detail. In this study we employed the 5xFAD mouse model of familial Alzheimer's disease crossed with mouse lines that selectively fluoresce in excitatory pyramidal cells (PCs) and inhibitory PV cells. We performed patch clamp recordings of PCs and three distinct PV cell sub-types to record the spiking activity and synaptic input during SWR events. Our findings support the hypothesis that a preferential reduction in synaptic input and activity of PV basket cells underlies downstream network alterations and suggest that long-term alterations to PC-PVBC micro-circuitry contribute to dysfunction in early amyloid pathology.

Materials and Methods

Experimental Animals

To record the activity of excitatory PCs and inhibitory PV cells in amyloid pathology, we employed a combined breeding strategy of transgenic and targeted knockin mice. Transgenic 5xFAD mice (RRID:MMRRC_034840-JAX) (Oakley et al., 2006) were back-crossed for over five generations to the C57BL/6J (RRID:IMSR_JAX:000664) background, which was common to all other strains used. To target the calcium activity of PCs under confocal microscopy, transgenic homozygous Thy1-GCaMP6f-GP5.5 (RRID:IMSR_JAX:024276) (Dana et al., 2014) were crossed with hemizygous 5xFAD mice to yield litters with both 5xFAD/+;Thy1-GCaMP6f/+ and Thy1-GCaMP6f/+ littermate controls. PV cells were identified by crossing double homozygous knockin PV^{Cre}/PV^{Cre};tdTom/tdTom (RRID:IMSR_JAX:008069, RRID:IMSR_JAX:007914) (Hippenmeyer et al., 2005; Madisen et al., 2010) with hemizygous 5xFAD mice to yield litters with both 5xFAD/+;PV^{Cre}/+;tdTom/+ and PV^{Cre}/+;tdTom/+ littermate controls. In a subset of experiments the reporter lines were crossed, yielding quadruple transgenic cohorts of 5xFAD/+;Thy1-GCaMP6f/+;PV^{Cre}/+;tdTom/+ and Thy1-GCaMP6f/+;PV^{Cre}/+;tdTom/+ littermate controls. Offspring were genotyped for 5xFAD genotype at age P7 by tail biopsy via automated genotyping services (Transnetyx, Cordoba, TN, USA). For all experiments, experimenters were blind to 5xFAD genotype until after data collection and analysis were fully complete. Mice were weaned at P21 and group housed in cages with 3-5 mice separated by sex. As a model of early amyloid pathology prior to neuronal or synaptic loss (Oakley et al., 2006), two experimental cohorts were chosen (each including both males and females) at 1 month (mo) and 3 mo of age (Table 1). Mice were kept on a standard 12 hr light/dark cycle, food and water were provided *ad libitum*, with all experimental procedures performed in accordance with the guidelines of the Georgetown University Animal Care and Use Committee.

Behavioral Testing

To test for hippocampal-dependent learning and memory deficits, mice were tested on the Barnes maze (Barnes, 1979), with some modifications. The Barnes maze was conducted on a white plastic apparatus (San Diego Instruments) 0.914 m in diameter, with overhead bright illumination (286 lx) serving as the aversive stimulus. The target hole was randomly selected, with four distal visual clues present for

97 visuospatial learning. The training phase consisted of four 180 s trials per day for 4 consecutive days.
98 The probe trial, in which the target hole was inaccessible, was conducted on the fifth consecutive day,
99 consisting of one 90 s trial. Mice were tracked using the ANY-maze tracking system, which was used for
100 distance and speed measurements. The primary measures of latency and number of entries to target
101 hole were hand-scored for increased reliability. Anxiety-like behavior was tested on the elevated plus
102 maze (Pellow et al., 1985). The mice could explore the maze for 5 min, in which time the number of
103 entries and fraction of time in the open arms were assessed by the ANY-maze tracking system. All tests
104 were conducted in the light cycle, at consistent times of the day for each mouse, in an enclosed behavior
105 room with 50 dB ambient sound and 23 lx ambient illumination. Males and females were run on the same
106 day, but in separate groups. Cohorts were not balanced by both sex and genotype, but as much as
107 possible testing order was prepared so that control and 5xFAD mice were alternated.

108 ***Acute Slice Preparation***

109 Brain slices were prepared using NMDG and HEPES-buffered artificial cerebrospinal fluid (aCSF)
110 following a protective recovery protocol (Ting et al., 2014, 2018). Briefly, mice were anesthetized with
111 isoflurane, transcardially perfused, dissected, and sliced in iced (0º C) NMDG-aCSF containing in mM:
112 92 NMDG, 2.5 KCl, 1.25 NaH_2PO_4, 30 $NaHCO_3$, 20 HEPES, 25 Glucose, 10 Sucrose, 5 Ascorbic Acid,
113 2 Thiourea, 3 Sodium Pyruvate, 5 N-acetyl-L-cysteine, 10 $MgSO_4$, 0.5 $CaCl_2$, pH to 7.3-7.4 with HCl (300-
114 310 Osm). All common reagents were obtained from Thermo Fisher Scientific. The brains were sliced
115 horizontally at 500 µm thickness with a Vibratome 3000 to preserve hippocampal micro-circuitry and
116 spontaneous SWRs. 3-4 slices were typically obtained per brain, which were bisected so that 6-8
117 hemislices in total were studied per animal. Slices spanned the dorsal-ventral axis, though were primarily
118 medial, as only horizontal slices with intact DG, CA3, and CA1 were retained, ranging from bregma 2-4
119 mm. The slices were transferred together to heated (33º C) NMDG-aCSF, in which Na^+ was gradually
120 introduced along an increasing concentration gradient every 5 min before transferring to room
121 temperature HEPES-aCSF containing in mM: 92 NaCl, 2.5 KCl, 1.25 NaH_2PO_4, 30 $NaHCO_3$, 20 HEPES,
122 25 Glucose, 5 Ascorbic Acid, 2 Thiourea, 3 Sodium Pyruvate, 5 N-acetyl-L-cysteine, 2 $MgSO_4$, 2 $CaCl_2$,

123 pH to 7.3-7.4 with NaOH (300-310 Osm). Slices recovered for 4 hours in a custom-built 150 mL incubation
124 chambers with circulating oxygenated HEPES-aCSF.

125 ***Slice Electrophysiology***

126 Slices were transferred to a Siskiyou PC-H perfusion chamber with a custom-built suspended Lycra
127 thread grid to allow perfusion below and above slice, modeled after (Hájos et al., 2009). Submerged
128 slices were anchored with Warner Instruments slice anchors so that they were sandwiched between two
129 grids, and perfused at a rate of 5 mL/min with heated (30º C) oxygenated aCSF containing in mM: 124
130 NaCl, 3.5 KCl, 1.2 NaH_2PO_4, 26 $NaHCO_3$, 10 Glucose, 1 $MgCl_2$, 2 $CaCl_2$, pH 7.3-7.4 (300-310 Osm).

131 Recordings were conducted with a Multiclamp 700B amplifier (Molecular Devices), digitized at 20
132 kHz and low-pass Bessel-filtered at 2 kHz with a personal computer running Clampex 11 and a DigiData
133 1440 (Molecular Devices). Two concurrent channels were captured: the local field potential (LFP) was
134 recorded with 0.5-1 MΩ borosilicate pipettes filled with aCSF, paired with 3-5 MΩ borosilicate pipettes for
135 cellular recordings. Cell-attached recordings were performed with aCSF + 5 μM Alexa Fluor® 488 nm
136 (Molecular Probes Cat# A-10440) or 594 nm (Molecular Probes Cat# A-10442) for pipette localization
137 under confocal microscopy. The selected concentration of Alexa dye was below reported alterations to
138 synaptic transmission (Maroteaux and Liu, 2016). Cell-attached recordings were followed with whole-cell
139 recordings of the same cell with a new pipette filled with a Cesium internal, containing in mM: 120
140 $CsMeSO_3$, 5 NaCl, 10 TEA•Cl, 10 HEPES, 1.1 EGTA, 4 QX314, 4 ATP•Na, 0.3 GTP•Na, pH to 7.2 with
141 CsOH (285 Osm). For pipette localization and *post hoc* morphological reconstruction, 5 μM Alexa (either
142 488 or 594 nm) and 0.5% wt/vl biocytin were added to the internal solution on the day of experiment.

143 The LFP electrode was placed in CA1 on the border of *stratum pyramidale* (*str. pyr.*) and *oriens*, a
144 location where both high amplitude sharp waves (SWs) and ripples are simultaneously detectable.
145 Recordings began 10 min after LFP electrode placement to allow slice to recover. If visually detectable
146 SWRs were not observed, the slice was logged as non-SWR producing (Table 1) and discarded. A
147 fluorescent cell was targeted for a loose (20-40 MΩ seal resistance) cell-attached recording of 3-5 min
148 duration. For Thy1-GCaMP6f slices, Ca^{2+} ensemble activity was recorded concurrently with a laser
149 scanning confocal microscope system (Thor Imaging Systems Division) equipped with 488/561/642 nm

150 lasers and green/red/far-red filters and dichroics mounted on an upright Eclipse FN1 microscope (Nikon
151 Instruments). One thousand 512 x 512 pixel frames were captured at a sample rate of 7.5 Hz. A 40x
152 water immersion objective was used, covering an imaging field of 350 x 350 μm, as a balance between
153 maximizing the imaging field while providing high enough magnification for patch clamp
154 electrophysiology.

155 Following the cell-attached recording, the same cell was targeted with a new Cesium internal
156 electrode. Upon reaching 1 GΩ seal resistance, the membrane was broken by a voltage pulse and quick
157 negative pressure. Access resistance was monitored periodically and recordings with a change >20%
158 were discarded. Putative excitatory post-synaptic currents (EPSCs) were measured in voltage-clamp at
159 a holding voltage of -70 mV, and putative inhibitory post-synaptic currents (IPSCs) in the same cell at 0
160 mV. Glutamatergic and GABAergic events were not pharmacologically isolated, as the primary goal was
161 to correlate synaptic activity with spontaneous SWRs, which would be affected by drug administration.
162 The reversal potentials of putative EPSCs and IPSCs matched closely with the expected glutamate and
163 GABA reversal potentials of 0 and -70 mV. This was determined by holding the cell from +20 to -100 mV
164 in 10 mV voltage steps and monitoring the current polarity inversion. Each voltage-clamp recording
165 ranged from 1-3 min. For PV cell recordings, the cell was then switched to current-clamp, with current
166 injection to offset the leak current and maintain a membrane potential of -70 mV. 35
167 hyperpolarizing/depolarizing steps of 5 pA increments were delivered to fill the cell with biocytin. A total
168 duration of at least 15 min of whole-cell configuration was maintained, after which an outside-out patch
169 was formed by slowly withdrawing the pipette.

170 ***Post Hoc Staining and Microscopy***

171 Slices with biocytin-filled PV cells were returned to the HEPES-aCSF incubation chamber for the
172 remainder of the day, then fixed overnight in 4% PFA, 4% glucose in PBS at 4° C. Slices then received
173 four 15 min PBS washes, 2 hours of permeabilization with 0.5% Triton-X in PBS, 2 PBS rinses, 3 hours
174 in Fluorescein-Avidin (1:500; Vector Laboratories Cat# A-2001, RRID:AB_2336455) in PBS, and four
175 additional 15 min PBS washes. Free floating slices were imaged with a laser scanning confocal
176 microscope system (Thor Imaging Systems Division). Under 20x magnification, z-stacks were obtained

177 covering the span of visible cellular processes (40-80 µm in 1 µm steps), for both green (biocytin) and
178 red (PV^{Cre}-tdTom) channels. In a subset of 14 slices (5 Control, 9 5xFAD from n_{mice} = 4 Control, 5 5xFAD),
179 an additional round of immuno-staining was performed for Ankyrin G, which labels the axon initial
180 segment of pyramidal cells. Antigen retrieval was performed on the 500 µm slices for 20 min in a steamer
181 with citrate buffer containing 10 mM $Na_3C_6H_5O_7$, 0.05% Tween20, and pH adjusted to 6.0 with HCl. Slices
182 were cooled to room temperature for 20 min in PBS, then blocked overnight with 10% NGS at 4° C. The
183 following day the slices were incubated with a primary monoclonal mouse antibody against Ankyrin G
184 (1:100; Thermo Fisher Scientific Cat# 33-8800, RRID:AB_2533145), 0.1% Tween20, 1% NGS in PBS.
185 After 48 hrs of primary incubation at 4° C, slices were given four 15 min PBS washes and incubated in
186 secondary containing Alexa Fluor® 647 conjugated goat anti-mouse IgG (1:500; Jackson
187 Immunoresearch Cat# 115-605-003, RRID:AB_2338902) and 1% NGS in PBS for 3 hrs at room
188 temperature. Slices were given four more 15 min PBS washes, rinsed in ddH_20, and mounted on slides
189 between silicone isolators with Vectashield® antifade mounting medium with DAPI (Vector Laboratories
190 Cat# H-1200, RRID:AB_2336790).

191 ***Pre-processing of Electrophysiology Data and Event Detection***

192 Pre-processing of files was conducted in Clampfit 11 (pClamp, Molecular Devices). Files for
193 calcium imaging experiments were trimmed around the confocal laser trigger signal for alignment of SWR
194 and calcium transients. Spikes were detected in cell-attached recordings with a 3 ms or 1.75 ms template
195 search for PCs or PV cells, respectively. A threshold of 6-8 was used (Clements and Bekkers, 1997) and
196 false negatives minimized (confirmed by manual inspection). False positives were removed by plotting
197 peak vs anti-peak amplitude to segregate noise from true spikes. Bursts were detected with the built-in
198 Burst Analysis, defined as three or more successive spikes, each within 60 or 40 ms (intra-burst interval)
199 for PCs or PV cells, respectively. Spike start, peak, and end times, burst start and end times, number of
200 events in burst, and intra-burst interval were exported from Clampfit for coincidence detection in
201 MATLAB.

202 Whole-cell recordings of post-synaptic current (PSC) signals were low-pass filtered below 1000 Hz
203 with a zero-phase Gaussian FIR filter. PSCs were detected with template searches. Multiple template

204 categories (3-4) of varying duration (ranging from 3-20 ms) were used to improve detection for
205 overlapping PSCs often seen around SWRs. Shorter duration templates used increasingly higher
206 thresholds, between 5-8, to minimize false negatives. Parameters were kept constant for each cell type.
207 PSC results including start, peak, and end times, amplitude, rise tau and decay tau were exported from
208 Clampfit and processed in Microsoft Excel to remove duplicate events with identical peak times. Limits
209 were set on rise and decay tau to remove false positives due to noise. Accepted EPSCs fell within a
210 range of 0.05-5 ms rise tau and 1-50 ms decay tau, while IPSCs fell within a range of 0.1-10 ms rise tau
211 and 3-100 ms decay tau.

212 ***Local Field Analysis and Sharp Wave Ripple Detection***

213 All analysis for coincidence detection between the LFP and cellular events was conducted with
214 custom-built MATLAB functions. Raw traces were imported using the abfload protocol
215 (https://github.com/fcollman/abfload). All applied filters were finite impulse response (FIR) Gaussian filter
216 with constant and corrected phase delays. A wide band-pass (1-1000 Hz) was first applied to remove
217 both low frequency DC drift and high frequency instrument noise. The detection of SWR events was
218 based upon prior approaches (Siapas and Wilson, 1998; Csicsvari et al., 1999; Eschenko et al., 2008),
219 with refinements to minimize false positives and permit additional analyses. The LFP was filtered in both
220 the sharp wave (SW: 1-30 Hz) and ripple (120-220 Hz) ranges, and the root mean square (RMS) was
221 computed every 5 ms in a 10 ms sliding window. The threshold for peak detection was set to 4 standard
222 deviation (SD) above the baseline (lower 0.95 quantile) RMS mean. Event start and end times were set
223 at 2 SD crossings. SWR events were defined as the intersection of concurrent SW and ripple events.
224 The duration of SWR events was determined from the union of concurrent SW and ripple events. The
225 peak of the SWR event was defined as the peak of the SW-RMS signal, and the amplitude as the
226 difference between the peak and baseline values of the SW signal. The power of the SW and ripple were
227 determined by the bandpower MATLAB function of the relevant filtered signal, which computes an
228 approximation of the integral of the power spectral density between the start and end times of the SWR
229 event. Additional filters were applied in the slow gamma (20-50 Hz) and fast/pathological ripple (250-500
230 Hz) ranges, and the power computed on a SWR-event basis, as the power of these SWR-nested

oscillations has been implicated in memory performance (Carr et al., 2012) and epileptogenesis (Foffani et al., 2007), respectively.

To visualize the spectral components of the LFP as a function of time, spectral analysis was performed for the duration of the recording as well as per SWR event via a Short-Time Fourier Transform (STFT) between 1-500 Hz. To better observe deviations from baseline power, the Z-score for each 1 Hz frequency band was calculated. A Fast-Fourier Transform (FFT) was also computed for a 200 ms window centered around each SWR peak and averaged across all events as an additional visualization of spectral power. The determination of the phase of slow gamma and ripple oscillations during SWRs was based on the analysis of (Varga et al., 2012). Within a 200 ms window centered around the SWR peak, the extrema of the filtered signal of interest were identified, and a piece-wise linear function fit with values from 0º to 180º between a maximum and minimum, 180º to 360º between a minimum and maximum, and then resetting to 0º. The number of cycles within the duration of the SWR event was recorded, from which the peak frequency was calculated as $n_{cycle}/SWR_{duration}$.

Pre-processing of Ca^{2+} Imaging Data

Raw time series were converted to the change in fluorescence normalized to baseline (*ΔF/F*) with custom-built ImageJ (FIJI) macros, in which batches of raw TIF images were imported with the Bio-Formats plugin (Open Microscopy Environment) and saved as TIF stacks. The TIF stacks were corrected for photo-bleaching via two iterations of the built-in Correct-Bleach plugin. Photo-bleaching was modeled as a sum of two exponentials, a fast 5 s decay and a slower decay over the duration of the recording (133 s). To assist in region-of-interest (ROI) placement, a semi-automated algorithm was applied to highlight regions of highest fluorescence change. For each TIF stack, the squared coefficient of variation (SCV) image was calculated, defined as the variance divided by the average squared for each pixel, or equivalently:

$$Img_{SCV} = \frac{1}{n}\sum_{i=1}^{n}\left(\frac{Img_i - \overline{Img}}{\overline{Img}}\right)^2$$

Circular ROIs were manually drawn over all identified cells in the SCV image and confirmed with the time series to encompass active cells. Notably, in this way only cells with variable fluorescence were

identified, and static highly fluorescent Ca^{2+}-loaded cells were excluded. The *ΔF/F* for each cell was calculated by first subtracting the background fluorescence F_b, defined as the lowest intensity pixel across the entire time series. F_0 for each ROI was defined as the average of the ten images with the lowest intensity. The *ΔF/F* was thus calculated as:

$$\Delta F_i / F_0 = \frac{F_i - F_0}{F_0 - F_b}$$

These values were exported from ImageJ, along with a separately calculated timing file for each image, computed from a threshold search in Clampfit of the confocal laser trigger channel.

Calcium Transient Detection and SWR Coincidence Analysis

Automatic detection of calcium transients was performed by first correcting for slow changes in fluorescence, either from remaining photo-bleaching or gradual drift of the imaging plane. A smoothed moving average, calculated with robust locally-weighted regression (Cleveland, 1979) with a window 25% of the file duration (33 s), was subtracted from each *ΔF/F* trace. The baseline-corrected *ΔF/F* traces were interpolated from the raw sampling rate of 7.5 Hz to 2 kHz, and the LFP downsampled from 20 kHz to 2 kHz for coincidence detection. Automatic threshold detection for each cell was set at 4 SD above baseline, with the start and end times for each event set at 2 SD. The baseline of each cell was determined by an iterative algorithm of gaussian fitting to the histogram of all data points, which for most cells was a skewed one-tailed distribution with a large baseline peak at zero and a long positive tail representing transient events. For uncommon cells without a skewed distribution (kurtosis < 0), a single gaussian fit was applied to the entire histogram, providing an estimate of the baseline mean and SD. However, for most cells, two iterations were employed, with the first a double-gaussian fit to the entire histogram. The higher amplitude gaussian SD was then used to constrain the upper limit on a second iteration single-gaussian refinement fit of only the baseline. Special logic was necessary in rare situations. For excessively skewed distributions (high *ΔF/F*, kurtosis > 5) the double-gaussian fit was constrained to the lower 0.95 quantile of data. For extremely active cells, because of the slow decay kinetics of GCaMP, the signal peak rivaled or exceeded the baseline peak in amplitude. For these cells, the more negative rather than the higher amplitude peak was used as an estimate of the baseline. In the situation where

283 two peaks were not clearly differentiated (peak separation < 0.1 $\Delta F/F$), the gaussian means and SDs
284 were averaged together to arrive at an estimate for constraining the second iteration.

285 Once the baseline mean, SD, and thresholds were determined for each cell, events were detected
286 on a cell-by-cell basis, and characteristics calculated including start, peak, and end times, IEI, duration,
287 amplitude, and frequency. The interpolated calcium traces were trimmed and aligned with the down-
288 sampled LFP trace. Each calcium transient was classified as SWR-coincident if there was any overlap
289 between the start and end of the calcium transient and the start and end of the SWR, otherwise it was
290 classified as spontaneous. Cellular participation during SWRs was assessed by constructing a simplified
291 event matrix with SWRs in one dimension, and cells in the other, with a zero or one if the cell reached
292 threshold during the SWR. For fields with five or more active cells, the ensemble diversity was assessed
293 by calculating the pairwise Jaccard Similarity index between SWR events, ranging from a value of zero
294 if two SWR events had no cells in common, to a value of one if all cellular participants were identical,
295 modeled after the analysis of (Miyawaki et al., 2014). The cell-cell pairwise index was also calculated,
296 ranging from zero if two cells never participated in the same SWR events, to one if they participated in
297 precisely the same SWRs. The cumulative distribution functions were determined for each recording as
298 well as for all recordings grouped together by considering all off-diagonal values in one half of the
299 symmetric similarity matrices.

300 ***Spike and SWR Coincidence Analysis***

301 Each spike/burst was classified as SWR-coincident if there was any overlap between the start and
302 end of the spike/burst and the start and end of the SWR, otherwise it was classified as spontaneous. To
303 examine spike rate in more detail around SWR events, the peri-SWR spike probability was calculated by
304 sorting all spikes that occurred within a 200 ms window centered around each SWR peak into 2 ms bins
305 and normalizing to all SWR events. Spike-phase coupling was determined by identifying the previously
306 calculated gamma and ripple phases at the spike peak time. Spike phase times were only considered for
307 further analysis if trough-peak amplitude exceeded 4 SD of the gamma or ripple signal.

308 ***Post-Synaptic Current and SWR Coincidence Analysis***

309 Each EPSC/IPSC was classified as SWR-coincident (swrEPSC/swrIPSC) if there was any overlap
310 between the start and end of the event and a 100 ms window centered around each SWR peak, otherwise
311 it was classified as spontaneous (sEPSC/sIPSCs). The more conservative window to classify
312 spontaneous events (compared to the calcium and spike analysis) better captured the buildup of
313 EPSCs/IPSCs preceding SWRs (Schlingloff et al., 2014). As events overlap and complicate detection
314 during SWRs, for quantification the current was integrated in a 100 ms window centered at the SWR
315 peak to determine the total charge (swrEPSQ/swrIPSQ). For a view of the temporal progression of
316 synaptic input during SWRs, the charge was also calculated by integrating a sliding 100 ms window every
317 2 ms in a 200 ms window centered around the SWR peak. PSC-LFP phase coupling during SWR events
318 was quantified by band-pass filtering the whole-cell channel in the low gamma (20-50 Hz) and ripple
319 (120-220 Hz) ranges, and cross-correlating the gamma and ripple signals between the whole-cell and
320 LFP channels.

321 ***Experimental Design and Statistical Analyses***

322 Most experiments in this study have been presented in a case-control experimental design, in which
323 data from 5xFAD mice are compared to littermate controls. With behavioral learning on the Barnes Maze
324 we have employed a longitudinal repeated measures (RM) design. In analyzing the impact of factors on
325 LFP activity in a large sample of *ex vivo* slices, we have taken a factorial design. All data were tested for
326 normality and lognormality via Shapiro-Wilks tests. If all groups were normally distributed, they were
327 analyzed with parametric tests (unpaired t-test, n-way ANOVA, n-way RM ANOVA) and have been
328 displayed on bar plots with error bars representing the mean ± SEM. If any group was not normally
329 distributed, the data have been presented on box-whisker or violin plots, with lines indicating median and
330 quartiles, and full error bars representing range. If all groups were lognormally distributed, the data were
331 log transformed, the results of which were analyzed with parametric tests, with the log-means compared.
332 For clarity, the original non-transformed data have been displayed in plots. If any group was neither
333 normal nor lognormal, non-parametric statistical tests of rank were employed. Circular data (phase
334 angles) were analyzed with a similar approach. Data were tested for non-uniformity via a Rayleigh test

335 to determine if they could be sampled from a von Mises (circular normal) distribution. If the Rayleigh test
336 reached significance for all groups, means were compared with the Watson-Williams test, otherwise a
337 circular median test was performed.

338 The particular statistical tests used are listed primarily in the figure legends, with some details in
339 the main text. Any values cited in the text are mean ± SEM. All *post hoc* multiple comparisons used the
340 Šidák correction. Within each plot all individual data points are presented. No data were excluded based
341 on their values, but only for experimental reasons (e.g. no SWRs present, excessive slice movement,
342 unstable patch clamp recording). The n is indicated in the text and figure legends, and differs between
343 experiment, either n_{mice}, n_{slice}, or n_{cell}. Raw p-values are displayed in plots; if less than a significance level
344 of 0.05 they are bold. Data originating from male or female mice are presented as closed or open circles
345 respectively. Sex differences were examined for some endpoints, but in general the experiments were
346 insufficiently powered to determine sex differences. A power analysis of the principal experiments was
347 performed based on preliminary data, guiding the number of animals/cells chosen.

348 Graphpad Prism 8 was used for all 1 and 2-sample statistical tests. Microsoft Excel and MATLAB
349 2019 were used for some simple calculations of mean, SD, SEM, ratio, and error propagation. n-way
350 ANOVAs were performed in the Statistics and Machine Learning Toolbox of MATLAB 2019. Non-
351 parametric factorial data were aligned and ranked with ARTool (Wobbrock et al., 2011), before running
352 ANOVAs. Circular statistics were run in the Circular Statistics Toolbox for MATLAB (Berens, 2009).

353 ***Code Accessibility***

354 All code is open-source and available in public repositories, including current versions in active
355 development (Github) as well as archival copies used for this manuscript (Zenodo). MATLAB functions
356 are available at https://github.com/acaccavano/SWR-Analysis (archival copy: DOI: 10.5281/zenodo.
357 3625236). ImageJ (FIJI) macros are available at https://github.com/acaccavano/deltaFoF (archival copy:
358 DOI: 10.5281/zenodo.3625130).

359 **Results**

360 ***Three month 5xFAD mice have a minor spatial memory impairment***

361 The 5xFAD model of familial Alzheimer's disease is an aggressive though useful model of amyloid
362 pathology, as it exhibits heavy amyloid accumulation in hippocampus and associated cortices, and is
363 accompanied with memory impairment (Oakley et al., 2006). 5xFAD mice are unimpaired in performance
364 on the T-maze at 2 months (mo) but become impaired by 4-5 mo when amyloid burden is greater (Oakley
365 et al., 2006). Interestingly, at 3 mo there is no evidence for neuronal or synaptic degeneration, while
366 several synaptic markers begin to decline at 4 mo and are significantly reduced from controls by 9 mo.
367 Here, we examined the performance of two cohorts of 5xFAD mice and littermate controls on the Barnes
368 Maze: a 1 mo cohort with minimal reported amyloid accumulation (Oakley et al., 2006), and a 3 mo cohort
369 (Table 1). Both cohorts learned the task, as seen by decreased latency to find escape hole over
370 progressive days of training (Fig. 1A-B). There were no differences observed in training between
371 genotype for either the 1 mo cohort (Fig. 1A) or the 3 mo cohort (Fig. 1B). On the probe day, 1 mo 5xFAD
372 had similar latencies to controls (Fig. 1C), while 3 mo 5xFAD mice had a significantly longer latency to
373 find the escape hole from 18.4 ± 7.6 s to 37.4 ± 9.8 s (Fig. 1D,E). The number of entries to the area of
374 the escape hole, another commonly reported endpoint, was not significantly different for either cohort (1
375 mo: $t_{(18)} = 0.735$, $p = 0.472$; 3 mo: $t_{(25)} = 0.691$, $p = 0.496$; unpaired t-tests). 5xFAD mice displayed no
376 obvious motor impairments, as the total distance traveled did not differ between genotype at either age
377 (1 mo: 3.98 ± 0.91 m (Control = CT), 3.77 ± 0.49 m (5xFAD), $t_{(18)} = 0.203$, $p = 0.842$; 3 mo: 3.98 ± 0.49
378 m (CT), 3.40 ± 0.49 m (5xFAD), $t_{(25)} = 0.816$, $p = 0.422$; unpaired t-tests), neither did the mean speed (1
379 mo: 4.4 ± 1.0 cm/s (CT), 4.2 ± 0.5 cm/s (5xFAD), $t_{(18)} = 0.186$, $p = 0.856$; 3 mo: 4.4 ± 0.6 cm/s (CT), 3.8
380 ± 0.5 cm/s (5xFAD), $t_{(25)} = 0.819$, $p = 0.420$; unpaired t-tests).

381 To test if this observed memory impairment could be attributed to altered anxiety-like behavior, the
382 cohorts were also tested on the Elevated Plus Maze. Neither age cohort showed a significant difference
383 in fraction of time spent in open arms (1 mo: 15.4 ± 2.2% (CT), 15.1 ± 0.9% (5xFAD), $t_{(18)} = 0.129$, $p =$
384 0.900; 3 mo: 10.7 ± 1.0 (CT), 9.3 ± 1.5 (5xFAD), $t_{(25)} = 0.848$, $p = 0.404$; unpaired t-tests), nor in number
385 of open arm entries (1 mo: 7.9 ± 0.6 (CT), 7.4 ± 0.6 (5xFAD), $t_{(18)} = 0.570$, $p = 0.576$; 3 mo: 9.2 ± 0.7

386 (CT), 7.5 ± 0.6 (5xFAD), $t_{(25)}$ = 1.863, p = 0.074; unpaired t-tests). Therefore, we concluded that 3 mo
387 5xFAD mice on our genetic background had a mild spatial memory impairment. As memory impairment
388 has been widely reported in 5xFAD mice at later ages (Oakley et al., 2006; Ohno, 2009; Tohda et al.,
389 2012), no further memory tasks were performed.

390 ***Sharp wave ripples are increased in 3 month 5xFAD mice***

391 As spatial memory relies heavily on the activity of the hippocampus, and sharp wave ripples
392 (SWRs) are critical for the consolidation of new memories (Buzsáki, 1986; Wilson and McNaughton,
393 1994), we next recorded spontaneous SWRs in hippocampal slices from control and 5xFAD mice (Fig.
394 2A-B). SWRs were recorded in multiple slices for each animal and averaged in both a 1 mo cohort (n_{mice}
395 = 10 CT, 10 5xFAD), and a 3 mo cohort (n_{mice} = 27 CT, 29 5xFAD, Table 1). In the 1 mo cohort, the SWR
396 event frequency did not differ (Fig. 2C), nor were there changes for any other LFP endpoints (data not
397 shown). However, in the 3 mo cohort, SWR event frequency was increased in 5xFAD mice versus
398 controls from 0.94 ± 0.07 Hz to 1.25 ± 0.08 Hz (Fig. 2C). We next verified if there was an altered
399 percentage of slices exhibiting SWRs in 5xFAD mice (Table 1), as this could underlie observed
400 differences in event frequency. While a 2-way ANOVA revealed a significant effect of 5xFAD genotype
401 ($F_{(1,72)}$ = 6.51, p = 0.0129) and age ($F_{(1,72)}$ = 5.21, p = 0.0254) on percentage of slices with SWRs, the
402 only significant difference observed when corrected for multiple comparisons was between control slices
403 at 1 mo and 3 mo (p = 0.0059, Šidák correction), while 3 mo slices did not differ between genotype (p =
404 0.882, Šidák correction). Therefore, the observed differences in 3 mo mice are not likely due to altered
405 viability of the slices.

406 In addition to an increased event frequency, SWR amplitude was increased by 58 ± 17% in 3 mo
407 5xFAD mice and surprisingly were 3.7 ± 1.2 ms shorter in duration (Fig. 2D). This decrease in duration
408 was likely attributable to both increased peak ripple frequency and decreased number of complete ripple
409 cycles (Fig. 2E), and is of interest as longer duration SWRs have been demonstrated to improve memory
410 (Fernández-Ruiz et al., 2019). Spectral features of SWRs also differed between genotype (Fig. 2F-J).
411 Low-gamma (20-50 Hz) nested within SWRs, speculated to play a role in coordinating CA3 and CA1
412 memory replay (Carr et al., 2012), was increased in 5xFAD mice (Fig. 2H). While the ripple peak

413 frequency was shifted (Fig. 2E,G), the total power within the frequency range 120-220 Hz was unchanged
414 (Fig. 2I). The power of fast or pathological ripples (250-500 Hz) did not differ between 5xFAD and control
415 slices (Fig. 2J), suggesting the increased activity in 5xFAD slices was distinct from epileptiform activity
416 (Foffani et al., 2007).

417 Spontaneous SWRs recordings were repeated in three separate 3 mo sub-cohorts with different
418 reporter mouse lines for subsequent patch-clamp and Ca^{2+} imaging experiments (Table 1). SWR
419 frequency increased in 5xFAD mice in both larger cohorts: PV^{Cre}/+;tdTom/+ mice (135 ± 18%, n_{mice} = 13
420 CT, 11 5xFAD) and Thy1-GCaMP6f mice (156 ± 21%, n_{mice} = 10 CT, 11 5xFAD). In the third smaller
421 Thy1-GCaMP6f;PV^{Cre}/+;tdTom/+ cohort, this increase was not observed (93 ± 18%, n_{mice} = 4 CT, 7
422 5xFAD). A 2-way ANOVA for 5xFAD genotype and reporter line revealed only a significant effect of
423 5xFAD genotype ($F_{(1,50)}$ = 5.407, p = 0.024) and not reporter line ($F_{(2,50)}$ = 1.500, p = 0.233) nor interaction
424 term ($F_{(2,50)}$ = 2.064, p = 0.138), therefore the data for the three sub-cohorts were combined into the
425 results presented in (Fig. 2). To test if sex, brain hemisphere, and dorsal-ventral slice position had an
426 effect, an additional 4-way ANOVA of all slices was performed. A small effect of 5xFAD genotype was
427 found (n_{slice} = 101 CT, 88 5xFAD; $F_{(1,178)}$ = 10.42, p = 0.0015), and a small effect of dorsal-ventral position
428 ($F_{(1,178)}$ = 10.46, p = 0.0015), with ventral slices (bregma 3-4 mm) 126 ± 12% the frequency of more dorsal
429 slices (bregma 2-3 mm) for both control and 5xFAD slices. Correcting for multiple comparisons, within
430 each genotype the difference between dorsal and ventral slices was not significant (D vs V: p = 0.078
431 (CT), p = 0.235 (5xFAD), Šidák correction). No significant effects were observed for sex ($F_{(1,178)}$ = 0.728,
432 p = 0.395), brain hemisphere ($F_{(1,178)}$ = 0.873, p = 0.351), nor any interaction terms.

433 ***Altered ensembles of pyramidal cells are recruited in 5xFAD slices***

434 The replay of pyramidal cell (PC) ensembles during SWRs is critical for the consolidation of spatial
435 memory (Wilson and McNaughton, 1994; Skaggs and McNaughton, 1996; Lee and Wilson, 2002; O'Neill
436 et al., 2008). Given the observed alterations to SWRs in 3 mo 5xFAD mice, we next sought to determine
437 if ensembles of PCs were also altered. The ensemble activity of PCs was recorded under confocal
438 microscopy in slices from 5xFAD/+;Thy1-GCaMP6f mice and Thy1-GCaMP6f littermate controls. Active
439 cells were detected with a semi-automated algorithm and both spontaneous and SWR-coincident Ca^{2+}

440 transient events were detected (Fig. 3A-B). Within 5xFAD slices, the number of active cells detected per
441 imaging field was increased from 17.0 ± 2.6 to 24.0 ± 1.6 cells in n_{slice} = 25 CT, 23 5xFAD (Fig. 3C).
442 Likewise, a greater number of cells were active during SWR events in 5xFAD slices (CT: 3.6 ± 0.6,
443 5xFAD: 4.9 ± 0.8 cells) (Fig. 3D). This increased cellular participation during SWRs may explain the
444 increased SWR amplitude in 5xFAD slices (Fig. 2D). While the total number of active as well as SWR-
445 coincident cells was increased, the fraction of SWR-coincident cells was unchanged between genotype
446 (20.0 ± 1.7% (CT) vs 18.9 ± 2.0% (5xFAD), $t_{(46)}$ = 0.755, p = 0.454, unpaired t-test). We next asked if
447 characteristics of the Ca^{2+} events differed between genotype, as an indirect measure PC firing activity.
448 Averaging across cells from each slice, no differences were found in the frequency, amplitude, nor
449 duration of Ca^{2+} transient events (Fig. 3E). This suggests that on an individual cell level, PCs exhibit
450 similar activity in 5xFAD mice as compared to controls, with differences only becoming apparent on the
451 ensemble level. Finally, we sought to determine if the cellular composition of PC ensembles was altered.
452 The pairwise similarity of cellular participation between SWR events showed a reduced degree of
453 similarity in PC ensembles during SWRs in 5xFAD, as compared to control slices (Fig. 3F-G), indicating
454 an increased repertoire of ensembles. Cell-cell similarity was also decreased in 5xFAD slices (Fig. 3H),
455 suggesting aberrant cell participation may be disrupting ensembles.

456 ***Pyramidal cell spiking is relatively unchanged in 5xFAD mice***

457 To test more directly if pyramidal cell activity was altered, GCaMP6f+ PCs (n_{cell} = 41 CT, 55 5xFAD)
458 were targeted for loose cell-attached recordings (Fig. 4A). The majority of cells (n_{cell} = 41 CT, 46 5xFAD)
459 came from 5xFAD;Thy1-GCaMP6f and Thy1-GCaMP6f littermate controls. A small number (n_{cell} = 9
460 5xFAD) came from 5xFAD;Thy1-GCaMP6f;PV^{Cre}/+;tdTom/+ mice, which labeled both excitatory PCs in
461 green and inhibitory PV cells in red. Spikes and bursts (three or more spikes each within 60 ms) were
462 delineated as spontaneous or SWR-coincident (Fig. 4B). Consistent with prior studies (Mizuseki and
463 Buzsáki, 2013), the distribution of spike rates was lognormal, however there were no genotype
464 differences during either spontaneous or SWR periods (Fig. 4C). In both control and 5xFAD mice the PC
465 spike rate increased during SWRs, by 217 ± 56% in controls and 187 ± 48% in 5xFAD mice. To examine
466 spike rate in more detail around SWR events, the peri-SWR spike probability was averaged across all

467 cells within each genotype, showing similar spiking probabilities between genotype (Fig. 4D). The rate of
468 spike bursts did not differ between genotype, although the intraburst interval was decreased from 13.5 ±
469 1.1 ms to 11.3 ± 0.6 ms (Fig. 4E), indicating that although PCs had the same number of spikes, in 5xFAD
470 mice they did spike faster within bursts. The percentage of cells with bursts did not differ between
471 genotype (97.6% CT, 96.1% 5xFAD; $\chi^2_{(1)} = 0.158$, $p = 0.691$; Chi-Squared Test). We also examined if
472 the fractional participation of PCs in SWRs differed, quantified as the fraction of spikes that occurred
473 during SWRs, and the fraction of SWRs that had one or more spikes. Neither endpoint differed between
474 genotype (Fig. 4F).

475 Finally, we examined the phase-locking of spikes in both the slow gamma and ripple ranges (Fig.
476 4G). Phase-locking of PCs to the trough of ripples has been widely reported *in vivo* (Ylinen et al., 1995;
477 Csicsvari et al., 1999; Le Van Quyen et al., 2008). However, phase-locking of PCs to SWR-nested slow
478 gamma has not been widely investigated. We also examined this endpoint considering the robust
479 increase we observed in slow gamma power in 5xFAD mice (Fig. 2H). In the gamma range there was a
480 significant phase-locking of spikes in control mice preceding the trough at 135° (108°-161° 95%), while
481 the mean phase of 158° (99°-217° 95%) for 5xFAD mice did not reach significance (Fig. 4H). In the ripple
482 range, cells were not significantly phase-locked for either genotype. However, in control mice, the mean
483 phase at the trough of 186° more closely matches prior findings than for 5xFAD mice, with a mean phase
484 of 239° following the trough (Fig. 4I). These results may indicate that spike-phase coupling is impaired in
485 5xFAD mice, though the lack of significant ripple phase-locking for either genotype suggests there may
486 be limitations to this analysis in our slice preparation, as this finding differs from the robust ripple phase-
487 locking observed *in vivo* (Ylinen et al., 1995; Csicsvari et al., 1999; Le Van Quyen et al., 2008). One
488 difference between our study and prior *in vivo* recordings is that the spikes and LFP were recorded from
489 different electrodes, while *in vivo* LFP and spikes are typically recorded from the same set of channels.
490 As ripples are highly localized events, the distance between electrodes may confound spatial phase
491 locking. Taken together with the Ca^{2+} imaging data, these results indicate relatively minimal alterations
492 to the spiking activity of PCs in 5xFAD slices. However, the large variability in spiking rate may mask
493 small differences in activity.

494 ***Pyramidal cells receive increased synaptic E/I ratio***

495 Following the cell-attached recording of spiking activity, the electrode was replaced with one
496 containing a Cesium-based internal solution and the same cell targeted for a whole-cell voltage-clamp
497 recording to detect excitatory and inhibitory post-synaptic currents (EPSCs and IPSCs) at -70 mV and 0
498 mV (Fig. 5), respectively. Events were sorted as spontaneous (sEPSCs/sIPSCs) or SWR-coincident
499 (swrEPSCs/swrIPSCs). sEPSC frequency and amplitude were unchanged across genotype (Fig. 5D),
500 but there was a 96.8 ± 23.4% increase in total excitatory charge during SWRs (swrEPSQ) in 5xFAD mice
501 (Fig. 5F). Considering we observed that SWRs in 5xFAD mice were larger in amplitude and recruited
502 more PCs, this was not an altogether surprising result. This increase indicates that the enlarged SWRs
503 were accompanied with increased excitatory synaptic activity, likely originating from the CA3 region. The
504 lack of any increase in spontaneous excitatory activity may also be consistent with our cell-attached
505 results showing that at least locally in CA1, PCs fired similarly across genotype. We also tested coupling
506 between synaptic currents and oscillations in the LFP by filtering both channels in the slow gamma and
507 ripple ranges (Fig. 5E) and correlating between channels. Both gamma and ripple LFP oscillations were
508 more strongly anti-correlated to synaptic activity in 5xFAD mice (Fig. 5G), which is expected if both
509 channels are of higher amplitude. Together these results suggest that excitatory synaptic input is
510 increased during SWRs in 5xFAD mice, consistent with expectations from the LFP and Ca^{2+} imaging
511 experiments.

512 In contrast, the frequency and normalized charge of sIPSCs were decreased in 5xFAD mice, while
513 the amplitude was unchanged (Fig. 5H). Unlike excitatory charge, the total inhibitory charge during SWRs
514 (swrIPSQ) did not significantly differ between genotype (Fig. 5J). In both genotypes, inhibitory currents
515 were positively correlated with both slow gamma and ripple, however unlike excitatory currents, there
516 was no genotype difference (Fig. 5K). Given the observed increase in SWR activity in 5xFAD mice, this
517 result suggests that inhibition is not scaling proportionally to the increased excitation, thus shifting the
518 synaptic E/I balance. We directly assessed this for both spontaneous and SWR-driven currents. During
519 both spontaneous and SWR periods, the synaptic E/I charge ratio was significantly increased (Fig. 5L-
520 M), though for different reasons. Outside of SWRs, the E/I ratio of spontaneous synaptic activity was

521 increased due to a decrease in inhibition, whereas during SWRs, it was driven principally by an increase
522 in excitation. To examine the temporal progression of synaptic input during SWRs, we calculated the
523 swrEPSQ and swrIPSQ in a sliding 100 ms window across the SWR peak, from which a time course of
524 the synaptic E/I ratio could be determined (Fig. 5N). There was an early peak in the synaptic E/I ratio for
525 5xFAD mice that was not present in controls (Fig. 5O), which can be attributed to a build-up in excitation
526 with a delayed increase in inhibition.

527 ***PV basket cells have selectively reduced spiking***

528 While there are numerous inhibitory cell sub-types in the CA1 region that could underlie a shift in
529 E/I synaptic input to PCs (Pelkey et al., 2017), we focused on parvalbumin-expressing (PV) interneurons,
530 as they are the most highly active during SWR events (Somogyi et al., 2014). We performed LFP + cell-
531 attached recordings in 5xFAD/+;PV^{Cre}/+;tdTom/+ and PV^{Cre}/+;tdTom/+ littermate control mice for n_{cell} =
532 54 CT, 37 5xFAD (Fig. 6A). A smaller number of cells (n_{cell} = 19 CT, 19 5xFAD) were recorded from
533 5xFAD;Thy1-GCaMP6f;PV^{Cre}/+;tdTom/+ and Thy1-GCaMP6f;PV^{Cre}/+;tdTom/+ littermate controls. One
534 complication with the PV cell population is that there are at least three distinct sub-types within CA1 *str.*
535 *pyr.*, which vary in function and axonal target: basket cells (PVBCs), which target perisomatic regions of
536 PCs, bistratified cells (PVBSCs), which target both apical and basal dendrites of PCs, and axo-axonic
537 cells (PVAACs), which selectively target the axon initial segment (AIS) (Fig. 6B). To distinguish these,
538 we morphologically reconstructed the cells *post hoc* after filling with biocytin in whole-cell configuration
539 (Fig. 6C) and sorted them by axonal target. While PVBSCs were easily distinguished from both PVBCs
540 and PVAACs (Fig. 6C.2), PVBCs (Fig. 6C.1) and PVAACs (Fig. 6C.3) can look quite similar, as their
541 axonal targets overlap and not all PVAACs exhibit the characteristic “chandelier” phenotype. To address
542 this, we also examined the spike rate. Both PVBCs and PVBSCs are known to strongly increase their
543 spike rate during SWRs (Lapray et al., 2012; Katona et al., 2014), while for PVAACs spike rate does not
544 increase (Viney et al., 2013). Thus, cells that had ambiguous PVBC/PVAAC morphology and no spike
545 rate increase during SWRs were sorted as PVAACs. In a subset of 14 slices (5 CT, 9 5xFAD from n_{mice}
546 = 4 CT, 5 5xFAD), we additionally stained for Ankyrin G, which labels the AIS, and confirmed
547 colocalization with two expected PVAACs (Fig. 6C.4). The proportion of cells sorted in this way matched

548 reasonably well with prior published findings of 60% PVBC, 25% PVBSC, 15% PVAAC in CA1 *str. pyr.*
549 (Baude et al., 2007) and did not significantly differ between genotype (Fig. 6D).

550 Based on these delineations, we observed that PVBCs had a selective and robust reduction in
551 spike rate during SWR periods, from 62.9 ± 10.6 Hz to 34.0 ± 6.2 Hz, whereas the PVBC spike rate did
552 not significantly differ during spontaneous periods (Fig. 7A.1). Spikes rates during both spontaneous and
553 SWR periods did not differ between genotype in PVBSCs (Fig. 7B.1) or PVAACs (Fig. 7C.1). As expected
554 from sorting the cell sub-types, spike rates increased during SWRS for both PVBCs (CT: 5.6 ± 1.2 fold,
555 5xFAD: 5.9 ± 2.4 fold, Fig. 7A.1) and PVBSCs (CT: 4.4 ± 1.2 fold, 5xFAD: 6.8 ± 5.0 fold, Fig. 7B.1), while
556 PVAACs only saw minor and non-significant increases (CT: 1.0 ± 0.4 fold, 5xFAD: 2.4 ± 0.8 fold, Fig.
557 7C.1). The peri-SWR spike probability revealed that in 5xFAD mice, PVBCs spikes fell in a significantly
558 narrower window (Fig. 7A.2), with a reduced full-width half-maximum value from 44 ± 19 ms to 18 ± 5
559 ms. Intriguingly, this narrower window of spiking in 5xFAD mice was accompanied by shorter duration
560 SWRs (Fig. 2D), suggesting the activity of these cells is critical for normal ripple progression. In contrast,
561 PVBSCs appeared to increase their firing after the SWR peak (Fig. 7B.2) in 5xFAD mice, perhaps playing
562 a compensatory role. PVAACs appeared to have decreased probability of spiking in 5xFAD mice,
563 particularly before the SWR peak (Fig. 7C.2). However, unlike PVBCs, neither PVBSCs nor PVAACs
564 showed significant genotype differences when corrected for multiple comparisons (Fig. 7A-C.2).

565 Considering the rate of bursts, defined as three or more spikes each within 40 ms, there was a
566 tendency for a reduction for PVBCs (Fig. 7A.3) and no change for PVBSCs (Fig. 7B.3) or PVAACs (Fig.
567 7C.3). No differences were observed in the proportion of cells that exhibited bursts for PVBCs (100% CT,
568 93.8% 5xFAD; $\chi^2_{(1)} = 0.842$, $p = 0.359$; χ^2 Test), PVBSCs (80.0% CT, 90.0% 5xFAD; $\chi^2_{(1)} = 0.288$, $p =$
569 0.591), or PVAACs (50.0% CT, 83.3% 5xFAD; $\chi^2_{(1)} = 1.500$, $p = 0.221$). In PVBCs, the fraction of SWRs
570 that coincided with a PV burst was significantly reduced from 65.4 ± 8.5% to 32.9 ± 8.5% (Fig. 7A.4),
571 while there was no genotype difference for PVBSCs (Fig. 7B.4) or PVAACs (Fig. 7C.4).

572 We also examined the spike phase-locking of these three PV cell types, as these have been
573 carefully studied *in vivo* for theta (8-12 Hz, during mobility) and ripple oscillations (Varga et al., 2014).
574 The precise temporal ordering of PV cell sub-types during network oscillations has been proposed to play

575 a critical role in the spatiotemporal control of PCs. During ripples, PVBCs have been observed to fire just
576 after the trough of the ripple, followed by PVBSCs and then PVAACs. Less studied is the phase-locking
577 of PV cells during SWR-nested slow gamma oscillations, which we examined as we observed alterations
578 in this endpoint for the PC population (Fig. 4H). We found significant gamma phase-locking of PVBCs for
579 5xFAD mice at 273° (247°-298° 95%), but not for control mice (Fig. 7A.6). PVBSCs were similarly gamma
580 phase-locked for 5xFAD mice at 292° (249°-336° 95%), but not for control mice (Fig. 7B.6). In contrast,
581 in PVAACs we observed phase-locking in control mice at 246° (224°-368° 95%), but not for 5xFAD mice
582 (Fig. 7C.6). While the precise significance of gamma phase-locking has yet to be demonstrated, these
583 genotype differences point to a temporal disordering of PV cell inhibition.

584 Within the ripple range, in PVBCs, there was a significant phase-locking in control mice at 228°
585 (198°-259° 95%), and in 5xFAD mice at 208° (186°-231° 95%), with no significant genotype difference
586 (Fig. 7A.7). These values are in line with prior *in vivo* studies, where 0° in our study was defined as the
587 peak of the ripple cycle and 180° as the trough. PVBSCs did not exhibit significant phase-locking in the
588 ripple range, although the average angles are line with *in vivo* studies (CT: 241°, 5xFAD: 225°) (Fig.
589 7B.7). PVAACs exhibited ripple phase preference for control mice at 257° (219°-296° 95%), in line with
590 *in vivo* studies. However, in 5xFAD mice, PVAACs spiked earlier, at 204° (164°-245° 95%) (Fig. 7C.7).
591 Although we observed no significant change in PVAAC spike rate, this disruption in temporal ordering
592 may still have downstream network consequences.

593 ***PV basket cells have selective decrease in excitatory synaptic drive and decreased E/I ratio***

594 Following cell-attached recording of spiking activity, the electrode was replaced with a Cesium
595 internal and the same PV cell was targeted for a whole-cell voltage-clamp recording (Fig. 8A). EPSCs
596 were recorded at -70 mV (Fig. 8B-D.1). Surprisingly, none of the three PV cell subtypes had any change
597 in spontaneous excitatory activity between genotype (Fig. 8B-D.2). However, PVBCs from 5xFAD mice
598 saw a 50.1 ± 10.7% reduction in excitatory charge during SWR events (Fig. 8B.3), whereas there was no
599 change for PVBSCs (Fig. 8C.3) or PVAACs (Fig. 8D.3). In a subset of cells, we also recorded IPSCs at
600 0 mV (Fig. 8E.1 for PVBCs, insufficient number of PVBSCs and PVAACs for analysis). Inhibitory input to
601 PVBCs was unchanged for both spontaneous (Fig. 8E.2) and SWR periods (Fig. 8E.3). This selective

602 decrease in excitation to PVBCs during SWRs, in contrast to the observation in PCs (Fig. 5F), resulted
603 in a significant decrease in the synaptic E/I ratio during SWRs, though not during spontaneous periods
604 (Fig. 8F-H). Since we recorded the cell-attached spiking activity from the same PVBCs, we were next
605 interested if reduced SWR spike rate (Fig. 7A.1) was correlated with altered synaptic E/I ratio during
606 SWRs. We observed a moderate positive correlation for control PVBCs, but no correlation between spike
607 rate and E/I ratio for 5xFAD PVBCs (Fig. 8I), suggesting that not only is excitatory synaptic input during
608 SWRs reduced, potentially through altered PC-PVBC connectivity, but there are also deficits in PVBC
609 input-output function, consistent with prior studies of intrinsic PV cell dysfunction (Verret et al., 2012).

610 **Discussion**

611 Here we identified a preferential impairment in PVBC function in a model of AD, while PVBSCs,
612 PVAACs, and excitatory PCs were relatively spared. By investigating the synaptic input and spike output
613 of these cell types, we present a careful description of hippocampal micro-circuitry alterations in early
614 amyloid pathology during activity critical for memory consolidation (i.e. SWRs). PVBCs displayed a
615 reduced synaptic E/I ratio during SWRs (Fig. 8G), driven by a reduction in excitatory synaptic input (Fig.
616 8F). PVBCs spiked less during SWRs (Fig. 7A.1), thus providing reduced inhibitory control to excitatory
617 PCs. In contrast, PCs displayed an increased synaptic E/I ratio (Fig. 5O), with similar spiking activity
618 between genotype (Fig. 4C). As the strong inhibition PVBCs provide is critical for the selection of PC
619 ensembles (Klausberger and Somogyi, 2008; Ellender et al., 2010), this selective reduction may explain
620 the enlarged PC ensembles (Fig. 3D), aberrant cellular participation (Fig. 3G), and more frequent and
621 larger amplitude SWRs in 5xFAD mice (Fig. 2C). Intriguingly, the increase in SWRs appears detrimental,
622 despite their role in memory consolidation, as we also observed spatial memory deficits (Fig. 1D).
623 Considering the surprising role SWRs play in down-regulating synapses and reducing memory-irrelevant
624 activity (Norimoto et al., 2018), these aberrant SWRs may be interfering with memory-relevant
625 reactivations. Several mechanisms likely contribute to the increase in SWRs. The reduction of sIPSCs
626 that PCs receive between SWRs (Fig. 5H) may permit the buildup of excitation necessary for SWR
627 initiation. The decreased duration of SWRs (Fig. 2D) may more quickly reset the system for subsequent
628 events. A more complete description would also require investigation of CA3 and CA2 micro-circuitry.

629 ***Hyperactivity and inhibitory disruption in Alzheimer's disease***

630 Our findings are consistent with growing evidence linking hyperactivity and Aβ aggregation (Zott et
631 al., 2018). Hippocampal hyperactivity is seen in mouse models of early amyloid pathology as increased
632 seizure risk (Palop et al., 2007) and enlarged ensemble activity (Busche et al., 2012). Our results extend
633 these findings to the study of SWRs. In addition, several studies have demonstrated that a preferential
634 disruption to inhibitory cells underlies hyperactivity (Verret et al., 2012; Hazra et al., 2013; Mahar et al.,
635 2016; Hijazi et al., 2019). In the clinical population, seizures are more prevalent and associated with
636 earlier onset of cognitive decline in amnestic MCI patients (Vossel et al., 2013). Additionally, task-related

637 engagement of the hippocampus, as tested via event-related fMRI, indicates hippocampal hyper-
638 activation in MCI patients relative to aged controls, while more progressed AD patients experience hypo-
639 activation (Dickerson et al., 2005; Pariente et al., 2005). These studies suggest our observed phenotype
640 may better model MCI rather than fully progressed AD.

641 ***Pyramidal cell diversity***

642 While this study focuses on inhibitory cell diversity, there is growing appreciation for PC diversity
643 in the hippocampus, and a delineation between calbindin-positive (CB+) superficial and CB- deep cells
644 (Valero et al., 2015; Soltesz and Losonczy, 2018). As PVBCs receive more innervation from superficial
645 PCs, and provide more inhibition to deep PCs (Lee et al., 2014), we expect a PVBC spike rate reduction
646 would asymmetrically affect the PC population. Our Thy1-GCaMP6f mice sparsely labeled both
647 superficial and deep PCs, and in more ventral hippocampus we observed CB+ expression in a bilayer as
648 previously observed (Baimbridge and Miller, 1982; Slomianka et al., 2011), complicating segregation
649 based purely on location. A combinatorial approach of $Calb^{Cre}$-tdTom and pan-glutamatergic GCaMP6f
650 expression would be a promising avenue to distinguish ensemble activity of these two PC subtypes.

651 ***Sharp wave ripple alterations in aging and disease***

652 In normal aging, SWR event and ripple frequency decrease (Wiegand et al., 2016; Cowen et al.,
653 2018), contrasting with the phenotype we observed in young adult mice. While it is accepted that AD is
654 distinct from accelerated aging (Toepper, 2017), similar decreases in SWRs have been observed in aged
655 AD models. In an apoE-ε4 knockin model of sporadic AD, SWR event frequency and gamma power are
656 reduced in 12-18 mo mice (Gillespie et al., 2016; Jones et al., 2019). Similarly, in 9-12 mo TgF344-AD
657 rats, SWR event frequency, power, and gamma power are reduced (Stoiljkovic et al., 2018). In younger
658 adults the findings are somewhat mixed. In a small cohort of 3 mo 5xFAD mice, SWR event frequency
659 and gamma power are reduced (Iaccarino et al., 2016). In 2-4 mo rTg4510 mice, SWR event frequency
660 is unchanged while amplitude and ripple power are reduced (Ciupek et al., 2015). Another study has
661 suggested a failure of PC-PV circuits in amyloid pathology is due to regulation of the GluA4 AMPA
662 receptor, resulting in more frequent SWRs with reduced ripple frequency in 3-4 mo APP_{swe}/PS1ΔE9 mice
663 (Xiao et al., 2017). Aside from effects on SWR event frequency, propagation of SWRs is also disrupted;

664 3 mo APP-PS1 mice show impaired propagation from CA3 to CA1 correlated with increased
665 immunoreactivity for PV (Hollnagel et al., 2019).

666 One notable difference between our study and many prior ones is the acute slice versus *in vivo*
667 preparation. Slice electrophysiology permits a careful study of the synaptic inputs to different neuronal
668 sub-types during SWRs, an infeasible task *in vivo*. The choice of AD model also surely has implications.
669 While the 5xFAD model has several advantages for this study, its primary disadvantage is APP
670 overexpression, common to all first-generation transgenic models. Some have noted electrophysiological
671 alterations are more related to APP overexpression than Aβ aggregation (Born et al., 2014). We
672 attempted to address this by examining a 1 mo cohort (preceding Aβ aggregation), in which APP
673 overexpression would still presumably have an effect, a cohort in which we observed no alterations (Fig.
674 1A,C,2C). There are fewer studies of second-generation APP knockin models which address the problem
675 of APP overexpression, yet have less pronounced disease phenotypes (Sasaguri et al., 2017). In one
676 relevant study, sIPSC amplitude from putative PV cells is decreased in parietal cortex PCs from 18-20
677 mo App^{NL-F} mice, although synaptic E/I balance is unchanged, perhaps through homeostatic mechanisms
678 (Chen et al., 2018). It will be critical to study hippocampal network alterations in novel AD mouse models
679 with greater validity as they become increasingly available.

680 ***Potential mechanisms for PVBC deficit***

681 Several mechanisms may underlie PVBC dysfunction in amyloid pathology. Intrinsic factors
682 including downregulation of the voltage-gated $Na_{v1.1}$ channel can explain decreased PV cell excitability
683 and cortical network hyperactivity (Verret et al., 2012). It remains to be shown if different PV sub-types
684 are differentially affected, but according to the Allen Brain Institute Cell Types Database, all identified
685 murine PV clusters express the Scn1a gene encoding $Na_{v1.1}$ (Lein et al., 2007). Another potential
686 mechanism is loss of peri-neuronal nets (PNNs), part of the extracellular matrix surrounding soma and
687 proximal dendrites that preferentially ensheathe PV cells (Kwok et al., 2011; Sorg et al., 2016). The
688 function of PNN is incompletely understood, but both enhances PV cell excitability and activity (Slaker et
689 al., 2015; Balmer, 2016). In a prior study, we observed degradation of PNN increases SWR event
690 frequency by ~50% (Sun et al., 2017), a similar magnitude effect as the current study. Additionally, the

691 selective reduction of excitatory input to PV cells (Fig. 8B.3) is consistent with the decrease in miniature
692 EPSCs in PV cells in a brevican knockout, a major component of PNN (Favuzzi et al., 2017). Moreover,
693 PNN staining is reduced in 3 mo Tg2576 mice (Cattaud et al., 2018). PNNs are more selectively located
694 around PVBCs (>90%) than PVBSCs (25-50%) or PVAACs (<10%) (Yamada and Jinno, 2015),
695 potentially explaining the specificity we observe. However, our experiments would also be consistent with
696 upstream deficits in excitatory input to PV cells. This reduction is unlikely to occur locally, as we observed
697 similar spiking yet enlarged ensembles in the CA1 PC population. In 4 mo Tg2576 mice, there is a
698 preferential degeneration of direct entorhinal input to CA1 PV cells; optogenetic restoration of this input
699 rescues synaptic and spatial learning deficits (Yang et al., 2016). The overall cause of disruption to PV
700 cells is likely from several contributing factors, and further studies are required to identify the most salient
701 impairment, and thus the most promising avenue for intervention.

702 ***Implications of PVBC specific deficit***

703 Here, we identified a preferential impairment in PVBC function, concurrent with altered network
704 activity. The selectivity of synaptic alterations in PVBCs suggest they may be a promising target for
705 intervention to restore hippocampal network activity in early amyloid pathology. Given the rapid evolution
706 of tools to manipulate activity in a cell-type specific manner, this finding is of particular importance
707 considering optogenetic (Iaccarino et al., 2016) and chemogenetic (Hijazi et al., 2019) approaches to
708 ameliorate memory decline in AD. A limitation of these strategies is that the PV^{Cre} driver will also target
709 PVBSCs and PVAACs, potentially leading to unintended off-target consequences in temporal
710 sequencing. Novel combinatorial approaches utilizing both Cre and Flp (He et al., 2016) provide a
711 promising avenue to selectively manipulate distinct neuronal sub-types. In conclusion, this study
712 investigated the synaptic input and spiking output of distinct cell-types over the course of SWR events,
713 providing insight into synaptic deficits in early amyloid pathology, and informing future attempts to
714 manipulate the hippocampal micro-circuit.

References

Amatniek JC, Hauser WA, DelCastillo-Castaneda C, Jacobs DM, Marder K, Bell K, Albert M, Brandt J, Stern Y (2006) Incidence and predictors of seizures in patients with Alzheimer's disease. Epilepsia 47:867–872.

Baimbridge KG, Miller JJ (1982) Immunohistochemical localization of calcium-binding protein in the cerebellum, hippocampal formation and olfactory bulb of the rat. Brain Research 245:223–229.

Balmer TS (2016) Perineuronal Nets Enhance the Excitability of Fast-Spiking Neurons. eNeuro 3.

Barnes CA (1979) Memory deficits associated with senescence: a neurophysiological and behavioral study in the rat. J Comp Physiol Psychol 93:74–104.

Baude A, Bleasdale C, Dalezios Y, Somogyi P, Klausberger T (2007) Immunoreactivity for the GABAA receptor alpha1 subunit, somatostatin and Connexin36 distinguishes axoaxonic, basket, and bistratified interneurons of the rat hippocampus. Cereb Cortex 17:2094–2107.

Berens P (2009) CircStat: A MATLAB Toolbox for Circular Statistics. Journal of Statistical Software 31:1–21.

Born HA, Kim J-Y, Savjani RR, Das P, Dabaghian YA, Guo Q, Yoo JW, Schuler DR, Cirrito JR, Zheng H, Golde TE, Noebels JL, Jankowsky JL (2014) Genetic suppression of transgenic APP rescues Hypersynchronous network activity in a mouse model of Alzeimer's disease. J Neurosci 34:3826–3840.

Braak H, Braak E (1991) Neuropathological stageing of Alzheimer-related changes. Acta Neuropathol 82:239–259.

Busche MA, Chen X, Henning HA, Reichwald J, Staufenbiel M, Sakmann B, Konnerth A (2012) Critical role of soluble amyloid-β for early hippocampal hyperactivity in a mouse model of Alzheimer's disease. PNAS 109:8740–8745.

Busche MA, Eichhoff G, Adelsberger H, Abramowski D, Wiederhold K-H, Haass C, Staufenbiel M, Konnerth A, Garaschuk O (2008) Clusters of hyperactive neurons near amyloid plaques in a mouse model of Alzheimer's disease. Science 321:1686–1689.

Buzsáki G (1986) Hippocampal sharp waves: their origin and significance. Brain Res 398:242–252.

742 Buzsáki G (2015) Hippocampal sharp wave-ripple: A cognitive biomarker for episodic memory and
743 planning. Hippocampus 25:1073–1188.
744 Buzsáki G, Leung LW, Vanderwolf CH (1983) Cellular bases of hippocampal EEG in the behaving rat.
745 Brain Res 287:139–171.
746 Buzsáki G, Logothetis N, Singer W (2013) Scaling brain size, keeping timing: evolutionary preservation
747 of brain rhythms. Neuron 80:751–764.
748 Carr MF, Karlsson MP, Frank LM (2012) Transient slow gamma synchrony underlies hippocampal
749 memory replay. Neuron 75:700–713.
750 Cattaud V, Bezzina C, Rey CC, Lejards C, Dahan L, Verret L (2018) Early disruption of parvalbumin
751 expression and perineuronal nets in the hippocampus of the Tg2576 mouse model of Alzheimer's
752 disease can be rescued by enriched environment. Neurobiol Aging 72:147–158.
753 Chen L, Saito T, Saido TC, Mody I (2018) Novel Quantitative Analyses of Spontaneous Synaptic Events
754 in Cortical Pyramidal Cells Reveal Subtle Parvalbumin-Expressing Interneuron Dysfunction in a
755 Knock-In Mouse Model of Alzheimer's Disease. eNeuro 5.
756 Ciupek SM, Cheng J, Ali YO, Lu H-C, Ji D (2015) Progressive Functional Impairments of Hippocampal
757 Neurons in a Tauopathy Mouse Model. J Neurosci 35:8118–8131.
758 Clements JD, Bekkers JM (1997) Detection of spontaneous synaptic events with an optimally scaled
759 template. Biophys J 73:220–229.
760 Cleveland WS (1979) Robust Locally Weighted Regression and Smoothing Scatterplots. Journal of the
761 American Statistical Association 74:829–836.
762 Colgin LL (2016) Rhythms of the hippocampal network. Nat Rev Neurosci 17:239–249.
763 Cowen SL, Gray DT, Wiegand J-PL, Schimanski LA, Barnes CA (2018) Age-associated changes in
764 waking hippocampal sharp-wave ripples. Hippocampus.
765 Csicsvari J, Hirase H, Czurkó A, Mamiya A, Buzsáki G (1999) Oscillatory Coupling of Hippocampal
766 Pyramidal Cells and Interneurons in the Behaving Rat. J Neurosci 19:274–287.
767 Dana H, Chen T-W, Hu A, Shields BC, Guo C, Looger LL, Kim DS, Svoboda K (2014) Thy1-GCaMP6
768 transgenic mice for neuronal population imaging in vivo. PLoS ONE 9:e108697.

769 Dickerson BC, Salat DH, Greve DN, Chua EF, Rand-Giovannetti E, Rentz DM, Bertram L, Mullin K, Tanzi
770 RE, Blacker D, Albert MS, Sperling RA (2005) Increased hippocampal activation in mild cognitive
771 impairment compared to normal aging and AD. Neurology 65:404–411.
772 Ego-Stengel V, Wilson MA (2010) Disruption of ripple-associated hippocampal activity during rest impairs
773 spatial learning in the rat. Hippocampus 20:1–10.
774 Ellender TJ, Nissen W, Colgin LL, Mann EO, Paulsen O (2010) Priming of Hippocampal Population Bursts
775 by Individual Perisomatic-Targeting Interneurons. J Neurosci 30:5979–5991.
776 Favuzzi E, Marques-Smith A, Deogracias R, Winterflood CM, Sánchez-Aguilera A, Mantoan L, Maeso P,
777 Fernandes C, Ewers H, Rico B (2017) Activity-Dependent Gating of Parvalbumin Interneuron
778 Function by the Perineuronal Net Protein Brevican. Neuron 95:639-655.e10.
779 Fernández-Ruiz A, Oliva A, Oliveira EF de, Rocha-Almeida F, Tingley D, Buzsáki G (2019) Long-duration
780 hippocampal sharp wave ripples improve memory. Science 364:1082–1086.
781 Foffani G, Uzcategui YG, Gal B, Menendez de la Prida L (2007) Reduced Spike-Timing Reliability
782 Correlates with the Emergence of Fast Ripples in the Rat Epileptic Hippocampus. Neuron 55:930–
783 941.
784 Gillespie AK, Jones EA, Lin Y-H, Karlsson MP, Kay K, Yoon SY, Tong LM, Nova P, Carr JS, Frank LM,
785 Huang Y (2016) Apolipoprotein E4 Causes Age-Dependent Disruption of Slow Gamma
786 Oscillations during Hippocampal Sharp-Wave Ripples. Neuron 90:740–751.
787 Girardeau G, Benchenane K, Wiener SI, Buzsáki G, Zugaro MB (2009) Selective suppression of
788 hippocampal ripples impairs spatial memory. Nat Neurosci 12:1222–1223.
789 Hájos N, Ellender TJ, Zemankovics R, Mann EO, Exley R, Cragg SJ, Freund TF, Paulsen O (2009)
790 Maintaining network activity in submerged hippocampal slices: importance of oxygen supply. Eur
791 J Neurosci 29:319–327.
792 Hauser WA, Morris ML, Heston LL, Anderson VE (1986) Seizures and myoclonus in patients with
793 Alzheimer's disease. Neurology 36:1226–1230.
794 Hazra A, Gu F, Aulakh A, Berridge C, Eriksen JL, Ziburkus J (2013) Inhibitory neuron and hippocampal
795 circuit dysfunction in an aged mouse model of Alzheimer's disease. PLoS ONE 8:e64318.

796 He M, Tucciarone J, Lee S, Nigro MJ, Kim Y, Levine JM, Kelly SM, Krugikov I, Wu P, Chen Y, Gong L,
797 Hou Y, Osten P, Rudy B, Huang ZJ (2016) Strategies and Tools for Combinatorial Targeting of
798 GABAergic Neurons in Mouse Cerebral Cortex. Neuron 91:1228–1243.
799 Hijazi S, Heistek TS, Scheltens P, Neumann U, Shimshek DR, Mansvelder HD, Smit AB, Kesteren RE
800 van (2019) Early restoration of parvalbumin interneuron activity prevents memory loss and
801 network hyperexcitability in a mouse model of Alzheimer's disease. Mol Psychiatry:1–19.
802 Hippenmeyer S, Vrieseling E, Sigrist M, Portmann T, Laengle C, Ladle DR, Arber S (2005) A
803 developmental switch in the response of DRG neurons to ETS transcription factor signaling. PLoS
804 Biol 3:e159.
805 Hollnagel J-O, Elzoheiry S, Gorgas K, Kins S, Beretta CA, Kirsch J, Kuhse J, Kann O, Kiss E (2019) Early
806 alterations in hippocampal perisomatic GABAergic synapses and network oscillations in a mouse
807 model of Alzheimer's disease amyloidosis. PLOS ONE 14:e0209228.
808 Iaccarino HF, Singer AC, Martorell AJ, Rudenko A, Gao F, Gillingham TZ, Mathys H, Seo J, Kritskiy O,
809 Abdurrob F, Adaikkan C, Canter RG, Rueda R, Brown EN, Boyden ES, Tsai L-H (2016) Gamma
810 frequency entrainment attenuates amyloid load and modifies microglia. Nature 540:230–235.
811 Jones EA, Gillespie AK, Yoon SY, Frank LM, Huang Y (2019) Early Hippocampal Sharp-Wave Ripple
812 Deficits Predict Later Learning and Memory Impairments in an Alzheimer's Disease Mouse Model.
813 Cell Rep 29:2123-2133.e4.
814 Jura B, Macrez N, Meyrand P, Bem T (2019) Deficit in hippocampal ripples does not preclude spatial
815 memory formation in APP/PS1 mice. Sci Rep 9:1–12.
816 Kamenetz F, Tomita T, Hsieh H, Seabrook G, Borchelt D, Iwatsubo T, Sisodia S, Malinow R (2003) APP
817 processing and synaptic function. Neuron 37:925–937.
818 Karlsson MP, Frank LM (2009) Awake replay of remote experiences in the hippocampus. Nat Neurosci
819 12:913–918.
820 Katona L, Lapray D, Viney TJ, Oulhaj A, Borhegyi Z, Micklem BR, Klausberger T, Somogyi P (2014)
821 Sleep and Movement Differentiates Actions of Two Types of Somatostatin-Expressing GABAergic
822 Interneuron in Rat Hippocampus. Neuron 82:872–886.

823 Klausberger T, Somogyi P (2008) Neuronal Diversity and Temporal Dynamics: The Unity of Hippocampal
824 Circuit Operations. Science 321:53–57.
825 Kudrimoti HS, Barnes CA, McNaughton BL (1999) Reactivation of hippocampal cell assemblies: effects
826 of behavioral state, experience, and EEG dynamics. J Neurosci 19:4090–4101.
827 Kwok JCF, Dick G, Wang D, Fawcett JW (2011) Extracellular matrix and perineuronal nets in CNS repair.
828 Dev Neurobiol 71:1073–1089.
829 Lapray D, Lasztoczi B, Lagler M, Viney TJ, Katona L, Valenti O, Hartwich K, Borhegyi Z, Somogyi P,
830 Klausberger T (2012) Behavior-dependent specialization of identified hippocampal interneurons.
831 Nature Neuroscience 15:1265–1271.
832 Le Van Quyen M, Bragin A, Staba R, Crépon B, Wilson CL, Engel J (2008) Cell type-specific firing during
833 ripple oscillations in the hippocampal formation of humans. J Neurosci 28:6104–6110.
834 Lee AK, Wilson MA (2002) Memory of sequential experience in the hippocampus during slow wave sleep.
835 Neuron 36:1183–1194.
836 Lee S-H, Marchionni I, Bezaire M, Varga C, Danielson N, Lovett-Barron M, Losonczy A, Soltesz I (2014)
837 Parvalbumin-Positive Basket Cells Differentiate Among Hippocampal Pyramidal Cells. Neuron
838 82:1129–1144.
839 Lein ES et al. (2007) Genome-wide atlas of gene expression in the adult mouse brain. Nature 445:168–
840 176.
841 Li Y, Sun H, Chen Z, Xu H, Bu G, Zheng H (2016) Implications of GABAergic Neurotransmission in
842 Alzheimer's Disease. Front Aging Neurosci 8:31.
843 Madisen L, Zwingman TA, Sunkin SM, Oh SW, Zariwala HA, Gu H, Ng LL, Palmiter RD, Hawrylycz MJ,
844 Jones AR, Lein ES, Zeng H (2010) A robust and high-throughput Cre reporting and
845 characterization system for the whole mouse brain. Nat Neurosci 13:133–140.
846 Mahar I, Albuquerque MS, Mondragon-Rodriguez S, Cavanagh C, Davoli MA, Chabot J-G, Williams S,
847 Mechawar N, Quirion R, Krantic S (2016) Phenotypic Alterations in Hippocampal NPY- and PV-
848 Expressing Interneurons in a Presymptomatic Transgenic Mouse Model of Alzheimer's Disease.
849 Front Aging Neurosci 8:327.

850 Maroteaux M, Liu SJ (2016) Alteration of AMPA Receptor-Mediated Synaptic Transmission by Alexa
851 Fluor 488 and 594 in Cerebellar Stellate Cells. eNeuro 3 Available at:
852 https://www.ncbi.nlm.nih.gov/pmc/articles/PMC4895128/ [Accessed July 26, 2018].
853 Mattson MP (2004) Pathways towards and away from Alzheimer's disease. Nature 430:631–639.
854 Miyawaki T, Norimoto H, Ishikawa T, Watanabe Y, Matsuki N, Ikegaya Y (2014) Dopamine receptor
855 activation reorganizes neuronal ensembles during hippocampal sharp waves in vitro. PLoS ONE
856 9:e104438.
857 Mizuseki K, Buzsáki G (2013) Preconfigured, skewed distribution of firing rates in the hippocampus and
858 entorhinal cortex. Cell Rep 4:1010–1021.
859 Nádasdy Z, Hirase H, Czurkó A, Csicsvari J, Buzsáki G (1999) Replay and Time Compression of
860 Recurring Spike Sequences in the Hippocampus. J Neurosci 19:9497–9507.
861 Nicole O, Hadzibegovic S, Gajda J, Bontempi B, Bem T, Meyrand P (2016) Soluble amyloid beta
862 oligomers block the learning-induced increase in hippocampal sharp wave-ripple rate and impair
863 spatial memory formation. Sci Rep 6:22728.
864 Norimoto H, Makino K, Gao M, Shikano Y, Okamoto K, Ishikawa T, Sasaki T, Hioki H, Fujisawa S,
865 Ikegaya Y (2018) Hippocampal ripples down-regulate synapses. Science:eaao0702.
866 Oakley H, Cole SL, Logan S, Maus E, Shao P, Craft J, Guillozet-Bongaarts A, Ohno M, Disterhoft J, Eldik
867 LV, Berry R, Vassar R (2006) Intraneuronal β-Amyloid Aggregates, Neurodegeneration, and
868 Neuron Loss in Transgenic Mice with Five Familial Alzheimer's Disease Mutations: Potential
869 Factors in Amyloid Plaque Formation. J Neurosci 26:10129–10140.
870 Ognjanovski N, Schaeffer S, Wu J, Mofakham S, Maruyama D, Zochowski M, Aton SJ (2017)
871 Parvalbumin-expressing interneurons coordinate hippocampal network dynamics required for
872 memory consolidation. Nat Commun 8:15039.
873 Ohno M (2009) Failures to reconsolidate memory in a mouse model of Alzheimer's disease. Neurobiol
874 Learn Mem 92:455–459.
875 O'Neill J, Senior TJ, Allen K, Huxter JR, Csicsvari J (2008) Reactivation of experience-dependent cell
876 assembly patterns in the hippocampus. Nat Neurosci 11:209–215.

877 Palop JJ, Chin J, Roberson ED, Wang J, Thwin MT, Bien-Ly N, Yoo J, Ho KO, Yu G-Q, Kreitzer A,
878 Finkbeiner S, Noebels JL, Mucke L (2007) Aberrant Excitatory Neuronal Activity and
879 Compensatory Remodeling of Inhibitory Hippocampal Circuits in Mouse Models of Alzheimer's
880 Disease. Neuron 55:697–711.
881 Palop JJ, Mucke L (2009) Epilepsy and cognitive impairments in Alzheimer disease. Arch Neurol 66:435–
882 440.
883 Palop JJ, Mucke L (2010) Amyloid-beta-induced neuronal dysfunction in Alzheimer's disease: from
884 synapses toward neural networks. Nat Neurosci 13:812–818.
885 Pariente J, Cole S, Henson R, Clare L, Kennedy A, Rossor M, Cipoloti L, Puel M, Demonet JF, Chollet
886 F, Frackowiak RSJ (2005) Alzheimer's patients engage an alternative network during a memory
887 task. Ann Neurol 58:870–879.
888 Pelkey KA, Chittajallu R, Craig MT, Tricoire L, Wester JC, McBain CJ (2017) Hippocampal GABAergic
889 Inhibitory Interneurons. Physiol Rev 97:1619–1747.
890 Pellow S, Chopin P, File SE, Briley M (1985) Validation of open:closed arm entries in an elevated plus-
891 maze as a measure of anxiety in the rat. J Neurosci Methods 14:149–167.
892 Pozueta J, Lefort R, Shelanski ML (2013) Synaptic changes in Alzheimer's disease and its models.
893 Neuroscience 251:51–65.
894 Roux L, Hu B, Eichler R, Stark E, Buzsáki G (2017) Sharp wave ripples during learning stabilize the
895 hippocampal spatial map. Nat Neurosci.
896 Sasaguri H, Nilsson P, Hashimoto S, Nagata K, Saito T, De Strooper B, Hardy J, Vassar R, Winblad B,
897 Saido TC (2017) APP mouse models for Alzheimer's disease preclinical studies. The EMBO
898 Journal 36:2473–2487.
899 Schlingloff D, Káli S, Freund TF, Hájos N, Gulyás AI (2014) Mechanisms of sharp wave initiation and
900 ripple generation. J Neurosci 34:11385–11398.
901 Serrano-Pozo A, Frosch MP, Masliah E, Hyman BT (2011) Neuropathological Alterations in Alzheimer
902 Disease. Cold Spring Harb Perspect Med 1:a006189.

903 Shankar GM, Li S, Mehta TH, Garcia-Munoz A, Shepardson NE, Smith I, Brett FM, Farrell MA, Rowan
904 MJ, Lemere CA, Regan CM, Walsh DM, Sabatini BL, Selkoe DJ (2008) Amyloid-beta protein
905 dimers isolated directly from Alzheimer's brains impair synaptic plasticity and memory. Nat Med
906 14:837–842.
907 Skaggs WE, McNaughton BL (1996) Replay of neuronal firing sequences in rat hippocampus during
908 sleep following spatial experience. Science 271:1870–1873.
909 Slaker M, Churchill L, Todd RP, Blacktop JM, Zuloaga DG, Raber J, Darling RA, Brown TE, Sorg BA
910 (2015) Removal of Perineuronal Nets in the Medial Prefrontal Cortex Impairs the Acquisition and
911 Reconsolidation of a Cocaine-Induced Conditioned Place Preference Memory. J Neurosci
912 35:4190–4202.
913 Slomianka L, Amrein I, Knuesel I, Sørensen JC, Wolfer DP (2011) Hippocampal pyramidal cells: the
914 reemergence of cortical lamination. Brain Struct Funct 216:301.
915 Soltesz I, Losonczy A (2018) CA1 pyramidal cell diversity enabling parallel information processing in the
916 hippocampus. Nat Neurosci 21:484–493.
917 Somogyi P, Katona L, Klausberger T, Lasztóczi B, Viney TJ (2014) Temporal redistribution of inhibition
918 over neuronal subcellular domains underlies state-dependent rhythmic change of excitability in
919 the hippocampus. Phil Trans R Soc B 369:20120518.
920 Sorg BA, Berretta S, Blacktop JM, Fawcett JW, Kitagawa H, Kwok JCF, Miquel M (2016) Casting a Wide
921 Net: Role of Perineuronal Nets in Neural Plasticity. J Neurosci 36:11459–11468.
922 Stoiljkovic M, Kelley C, Stutz B, Horvath TL, Hajós M (2018) Altered Cortical and Hippocampal Excitability
923 in TgF344-AD Rats Modeling Alzheimer's Disease Pathology. Cereb Cortex.
924 Sun ZY, Bozzelli PL, Caccavano A, Allen M, Balmuth J, Vicini S, Wu J-Y, Conant K (2017) Disruption of
925 perineuronal nets increases the frequency of sharp wave ripple events. Hippocampus.
926 Ting JT, Daigle TL, Chen Q, Feng G (2014) Acute brain slice methods for adult and aging animals:
927 application of targeted patch clamp analysis and optogenetics. Methods Mol Biol 1183:221–242.

928 Ting JT, Lee BR, Chong P, Soler-Llavina G, Cobbs C, Koch C, Zeng H, Lein E (2018) Preparation of
929 Acute Brain Slices Using an Optimized N-Methyl-D-glucamine Protective Recovery Method. J Vis
930 Exp.
931 Toepper M (2017) Dissociating Normal Aging from Alzheimer's Disease: A View from Cognitive
932 Neuroscience. Journal of Alzheimer's Disease 57:331–352.
933 Tohda C, Urano T, Umezaki M, Nemere I, Kuboyama T (2012) Diosgenin is an exogenous activator of
934 1,25D_3-MARRS/Pdia3/ERp57 and improves Alzheimer's disease pathologies in 5XFAD mice. Sci
935 Rep 2:535.
936 Valero M, Cid E, Averkin RG, Aguilar J, Sanchez-Aguilera A, Viney TJ, Gomez-Dominguez D, Bellistri E,
937 de la Prida LM (2015) Determinants of different deep and superficial CA1 pyramidal cell dynamics
938 during sharp-wave ripples. Nat Neurosci 18:1281–1290.
939 Varga C, Golshani P, Soltesz I (2012) Frequency-invariant temporal ordering of interneuronal discharges
940 during hippocampal oscillations in awake mice. Proc Natl Acad Sci USA 109:E2726-2734.
941 Varga C, Oijala M, Lish J, Szabo GG, Bezaire M, Marchionni I, Golshani P, Soltesz I (2014) Functional
942 fission of parvalbumin interneuron classes during fast network events. eLife 3:e04006.
943 Ven GM van de, Trouche S, McNamara CG, Allen K, Dupret D (2016) Hippocampal Offline Reactivation
944 Consolidates Recently Formed Cell Assembly Patterns during Sharp Wave-Ripples. Neuron
945 92:968–974.
946 Verret L, Mann EO, Hang GB, Barth AMI, Cobos I, Ho K, Devidze N, Masliah E, Kreitzer AC, Mody I,
947 Mucke L, Palop JJ (2012) Inhibitory interneuron deficit links altered network activity and cognitive
948 dysfunction in Alzheimer model. Cell 149:708–721.
949 Viney TJ, Lasztoczi B, Katona L, Crump MG, Tukker JJ, Klausberger T, Somogyi P (2013) Network state-
950 dependent inhibition of identified hippocampal CA3 axo-axonic cells *in vivo*. Nature Neuroscience
951 16:1802–1811.
952 Vossel KA, Beagle AJ, Rabinovici GD, Shu H, Lee SE, Naasan G, Hegde M, Cornes SB, Henry ML,
953 Nelson AB, Seeley WW, Geschwind MD, Gorno-Tempini ML, Shih T, Kirsch HE, Garcia PA, Miller

954 BL, Mucke L (2013) Seizures and epileptiform activity in the early stages of Alzheimer disease.
955 JAMA Neurol 70:1158–1166.
956 Wiegand J-PL, Gray DT, Schimanski LA, Lipa P, Barnes CA, Cowen SL (2016) Age Is Associated with
957 Reduced Sharp-Wave Ripple Frequency and Altered Patterns of Neuronal Variability. J Neurosci
958 36:5650–5660.
959 Wilson MA, McNaughton BL (1994) Reactivation of hippocampal ensemble memories during sleep.
960 Science 265:676–679.
961 Wobbrock JO, Findlater L, Gergle D, Higgins JJ (2011) The Aligned Rank Transform for Nonparametric
962 Factorial Analyses Using Only Anova Procedures. In: Proceedings of the SIGCHI Conference on
963 Human Factors in Computing Systems, pp 143–146 CHI '11. New York, NY, USA: ACM. Available
964 at: http://doi.acm.org/10.1145/1978942.1978963 [Accessed December 12, 2019].
965 Xiao M-F et al. (2017) NPTX2 and cognitive dysfunction in Alzheimer's Disease. Elife 6.
966 Yamada J, Jinno S (2015) Subclass-specific formation of perineuronal nets around parvalbumin-
967 expressing GABAergic neurons in Ammon's horn of the mouse hippocampus. J Comp Neurol
968 523:790–804.
969 Yang X, Yao C, Tian T, Li X, Yan H, Wu J, Li H, Pei L, Liu D, Tian Q, Zhu L-Q, Lu Y (2016) A novel
970 mechanism of memory loss in Alzheimer's disease mice via the degeneration of entorhinal-CA1
971 synapses. Mol Psychiatry.
972 Ylinen A, Bragin A, Nadasdy Z, Jando G, Szabo I, Sik A, Buzsaki G (1995) Sharp wave-associated high-
973 frequency oscillation (200 Hz) in the intact hippocampus: network and intracellular mechanisms.
974 J Neurosci 15:30–46.
975 Zott B, Busche MA, Sperling RA, Konnerth A (2018) What Happens with the Circuit in Alzheimer's
976 Disease in Mice and Humans? Annu Rev Neurosci 41:277–297.
977

978 **Legends**

979 **Table 1: *Mouse cohorts used in study***. *Top*, Electrophysiology/imaging cohorts were distinct from
980 behavioral cohorts. For both experiments, mice were studied at an age of 1 and 3 months (mo). *Bottom*,
981 The 3 mo electrophysiology/imaging cohort consisted of three sub-cohorts with different reporter genes.

982 **Figure 1:** ***Three month (mo) 5xFAD mice have a minor spatial memory impairment***. 1 mo (n_{mice} = 10
983 Control (CT), 10 5xFAD) and 3 mo (n_{mice} = 15 CT, 12 5xFAD) cohorts were trained on the Barnes Maze,
984 consisting of four days of training, each with four 180 s trials (***A,B***) and a final 90 s probe trial on the fifth
985 day (***C,D***). ***A,*** 1 mo control and 5xFAD mice learned the task, as seen through a decreased latency to
986 find the target escape hole and a significant effect of training day ($F_{(3,54)}$ = 23.89, p = 5.7 × 10^{-10}; 2-way
987 RM ANOVA, align-rank transformed). Each data point represents the day average of four trials of the
988 latency to enter the target. No genotype difference was observed ($F_{(1,18)}$ = 0.096, p = 0.760), nor was
989 there a significant interaction of genotype × training day ($F_{(3,54)}$ = 0.496, p = 0.687). ***B,*** 3 mo control and
990 5xFAD mice similarly learned the task ($F_{(3,75)}$ = 31.56, p = 2.7 × 10^{-13}; 2-way RM ANOVA, align-rank
991 transformed), with no significant effect of genotype ($F_{(1,25)}$ = 1.086, p = 0.307), nor interaction of genotype
992 × training day ($F_{(3,75)}$ = 0.983, p = 0.405). ***C,*** Latency to reach covered target hole on the 5th day probe for
993 1 mo cohort. No genotype difference was observed ($t_{(18)}$ = 0.212, p = 0.835; unpaired t-test, log
994 transformed). ***D,*** The latency on the final probe day for 3 mo mice was significantly increased ($t_{(25)}$ =
995 2.566, p = 0.0167; unpaired t-test, log transformed). ***E***, Representative heat map for 3 mo animals on the
996 final probe trial. Warmer colors represent longer duration. Control mice spent more time at the target and
997 surrounding region than 5xFAD mice. For all plots, individual data points represent an animal. Closed
998 circles represent males, open circles females. Box-whisker plots represent non-normal data as Median
999 and IQRs. p-values indicated above brackets.

1000 **Figure 2**: ***Sharp wave ripples are increased in 3 month 5xFAD mice***. ***A***, SWRs were recorded in acute
1001 horizontal slices with the LFP electrode located in CA1. ***B***, Example traces of 3 mo control (*left*) and
1002 5xFAD (*right*) slices. *1st trace*, LFP filtered between 1-1000 Hz, raster below indicates detected SWR
1003 events as overlap of sharp wave (SW) and ripple events. *2nd trace*, SW, filtered between 1-30 Hz, raster
1004 below indicates detected SW events. *3rd trace*, low gamma, filtered between 20-50 Hz. *4th trace*, ripple,
1005 filtered between 120-220 Hz, raster below indicates detected ripple events. *Bottom*, z-scored time-
1006 frequency spectrogram from 1-250 Hz. ***C***, SWR event frequency for 5xFAD and littermate controls for
1007 both 1 mo and 3 mo cohorts. *Left*, No difference was observed in the 1 mo cohort (n_{mice} = 10 CT, 10
1008 5xFAD; $t_{(18)}$ = 0.946, p = 0.357; unpaired t-test). *Right*, there was a significant increase in SWR event
1009 frequency in 3 mo 5xFAD mice (n_{mice} = 27 CT, 29 5xFAD; $t_{(54)}$ = 2.887, p = 0.006; unpaired t-test). ***D***, In
1010 3 mo 5xFAD mice, SWR event amplitude was increased ($t_{(48.9)}$ = 3.592, p = 0.0008; Welch's t-test) and
1011 of shorter duration ($t_{(54)}$ = 3.175, p = 0.0025; unpaired t-test). ***E***, In 3 mo 5xFAD mice the peak ripple
1012 frequency was increased ($t_{(54)}$ = 3.422, p = 0.0012; unpaired t-test), and the number of ripple cycles
1013 reduced ($t_{(54)}$ = 3.480, p = 0.0163; unpaired t-test). ***F***, Example SWR events for traces displayed in ***B***,
1014 with average z-scored time-frequency spectrogram of all events below. ***G***, Average Fast-Fourier
1015 Transform (FFT) of 200 ms window around all SWR events from characteristic subset of n_{slice} = 7 CT, 7
1016 5xFAD from n_{mice} = 4 CT, 5 5xFAD. Shaded region represents SEM. ***H***, In 3 mo 5xFAD mice, low gamma
1017 (20-50 Hz) power was increased (U = 193, p = 0.0009, Mann-Whiney), while ***I***, ripple power (120-220 Hz)
1018 and ***J***, fast ripple (250-500 Hz) were unchanged (U = 358, p = 0.591; U = 379, p = 0.845; Mann-Whitney).
1019 Note that in ***H***, one value was identified as an outlier by the ROUT method but was retained in analysis,
1020 as the data point appeared valid, and even with removal did not alter the observed increase (U = 193, p
1021 = 0.0015; Mann-Whitney). For all plots, individual data points represent the average of all slices recorded
1022 from an animal (n_{slice}/animal in Table 1). Closed circles represent males, open circles females. Bar plots
1023 indicate normal data with Mean ± SEM. Box-whisker plots represent non-normal data with Median and
1024 IQRs. p-values indicated above brackets.

1025 **Figure 3**: ***Altered ensembles of pyramidal cells are recruited in 5xFAD slices***. ***A***, *Top*, Confocal
1026 imaging of PC ensembles were recorded concurrently with SWRs. *Middle*, Example frame of time series.
1027 *Bottom,* Semi-automated algorithm to identify active cells, from which ROIs were drawn to extract ΔF/F.
1028 Scale bars = 50 μm. ***B***, Example LFP and ΔF/F for identified cells in slices from 3 mo control (*left*) and
1029 5xFAD (*right)* mice*. Top trace,* LFP trace with identified SWR events in raster below. Green SWR events
1030 signify there was at least one cell with a concurrent Ca^{2+} transient, gray indicates there were no cells
1031 active. *Middle green traces*, individual ΔF/F for each cell. *Bottom raster*, identified Ca^{2+} events above
1032 threshold. Dark colored event (blue or black) indicate concurrence with SWR, light gray indicates
1033 spontaneous event. ***C***, The total number of active cells was increased in 5xFAD slices (n_{slice} = 25 CT, 23
1034 5xFAD; $t_{(31.2)}$ = 3.091, p = 0.0042; Welch's t-test, log transformed), as well as ***D***, the number of cells active
1035 during SWRs ($t_{(40.1)}$ = 2.063, p = 0.046; Welch's t-test, log-transformed). ***E***, Ca^{2+} transient events averaged
1036 across cells for each slice, showed no differences between genotype, with no significant difference
1037 observed in frequency ($t_{(46)}$ = 0.616, p = 0.541; unpaired t-test), amplitude ($t_{(46)}$ = 0.176, p = 0.861;
1038 unpaired t-test), or duration ($t_{(46)}$ = 1.021, p = 0.312; unpaired t-test, log transformed). ***F***, *Top*, Event matrix
1039 displaying for one example recording, the SWR events on the x-axis, and cells on the y-axis. *Bottom left*,
1040 pairwise Jaccard similarity between SWR events (columns in event matrix). Similarity matrix is symmetric
1041 and the diagonal = 1 by definition—these have not been plotted for clarity. *Bottom right*, pairwise Jaccard
1042 similarity between cells (rows in event matrix). ***G***, Cumulative distribution function for all pairwise
1043 correlations from all slices between SWRs. SWR-SWR correlations revealed that ensembles were less
1044 correlated in 5xFAD slices ($n_{SWR\text{-}SWR}$ = 152880 CT, 396292 5xFAD; D = 0.179, $p < 10^{-15}$; Kolmogorov-
1045 Smirnov). Note that curves do not start at origin, as a substantial proportion of SWR-SWR pairs have no
1046 cells in common (22.7% CT, 40.6% 5xFAD). ***H***, Cell-cell correlations were also reduced for 5xFAD slices
1047 ($n_{cell\text{-}cell}$ = 5560 CT, 7170 5xFAD; D = 0.133, $p < 10^{-15}$; Kolmogorov-Smirnov). Individual data points
1048 represent a slice. Closed circles represent slices from males, open circles females. Bar plots indicate
1049 normal data with Mean ± SEM. Box-whisker plots represent non-normal data with Median and IQRs. p-
1050 values indicated above brackets.

1051 **Figure 4**: ***Pyramidal cell spiking is relatively unchanged in 5xFAD mice. A***, Diagram of a loose cell-
1052 attached recording of spikes from a GCaMP+ PC paired with LFP recording of SWRs. ***B***, Example traces
1053 from 3 mo control (*left*) and 5xFAD (*right*) slice. *Top trace*, LFP with SWR events in raster below. Gray
1054 shaded events indicate spontaneous SWR. Green shading indicates SWR coincident with at least one
1055 spike. Dark green shading indicates SWR coincident with burst, defined as 3 or more spikes each within
1056 60 ms. *Bottom trace*, Cell-attached recording from PC. Detected spikes and bursts indicated in raster
1057 below. Dark shading indicates they are coincident with SWR event, light gray shading indicates
1058 spontaneous events. ***C***, Spike rate during spontaneous and SWR periods. No effect of genotype was
1059 observed (n_{cell} = 41 CT, 55 5xFAD; $F_{(1,94)} = 0.542$, $p = 0.464$; 2-way RM ANOVA, align-rank transformed—
1060 zero-values preclude log-transform). No differences were observed during spontaneous ($p = 0.982$;
1061 Mann-Whitney *post hoc*, Šidák correction) or SWR periods ($p = 0.547$; Mann-Whitney *post hoc*, Šidák
1062 correction). PC spike rate significantly increased during SWRs, with a significant effect of
1063 spontaneous/SWR time period ($F_{(1,94)} = 27.17$, $p = 1.1 \times 10^{-6}$; 2-way RM ANOVA), both in control ($p =$
1064 0.0079; Wilcoxon *post hoc*, Šidák correction) and 5xFAD mice ($p = 0.00001$, Wilcoxon *post hoc*, Šidák
1065 correction). There was no significant interaction of genotype × period ($F_{(1,94)} = 1.393$, $p = 0.241$). ***D***, Peri-
1066 SWR spike probability. Dark lines indicate average of all cells within a genotype, shaded regions indicate
1067 SEM. There was no effect of genotype ($F_{(1,9500)} = 0.722$, $p = 0.396$; 2-way ANOVA), nor interaction of
1068 genotype × bin ($F_{(99,9500)} = 0.869$, $p = 0.819$; 2-way ANOVA). ***E***, The burst rate did not differ between
1069 genotype ($U = 998$, $p = 0.276$; Mann-Whitney), while the intra-burst interval was decreased ($U = 793$, p
1070 $= 0.028$; Mann-Whitney). ***F***, *left*, The fraction of spikes that occurred during SWRs was unchanged ($U =$
1071 999, $p = 0.3438$; Mann-Whitney), as well as *right*, the fraction of SWRs that had one or more spikes ($U =$
1072 1019, $p = 0.4244$; Mann-Whitney). ***G***, Example of SWR (*top trace*), with filtered slow gamma (20-50 Hz)
1073 and ripple (120-220 Hz) signals (*middle traces*). The phase of oscillations was set at 0° at peaks and
1074 180° at troughs. *Bottom trace*, cell-attached recording, with spike times marked by vertical dashed lines.
1075 ***H***, Polar phase plots of phase-locking of spikes to SWR-nested slow gamma. The angles of individual
1076 data points represent the average phase of all spikes for a cell. Length from origin (0-1) indicates the
1077 degree of phase-locking. A length of 1 signifies perfect phase-locking (every spike at same phase); a

1078 length of 0 indicates random or no phase-locking. Spikes were phase-locked in the gamma range in CT
1079 mice (Z = 8.28, p = 0.0001; Raleigh's test), though not for 5xFAD mice (Z = 2.60, p = 0.074; Raleigh's
1080 test). The median phase angles differed between genotype (P = 6.82, p = 0.009; Circular median test). ***I***,
1081 No phase-locking was observed in the ripple range for either genotype (CT: Z = 1.23, p = 0.296; 5xFAD:
1082 Z = 1.42, p = 0.244; Raleigh's test), nor did the median phase angle differ (P = 1.05, p = 0.306; Circular
1083 median test). Individual data points represent a cell. Closed circles represent cells from males, open
1084 circles females. Violin plots represent non-normal data as Median and IQRs. p-values indicated above
1085 brackets.
1086

1087 **Figure 5**: ***Pyramidal cells receive increased synaptic E/I ratio***. ***A***, Example traces of LFP + whole-cell
1088 recording voltage-clamped at -70 mV. Excitatory post-synaptic potentials (EPSCs) were sorted as
1089 spontaneous (sEPSCs) or SWR-coincident (swrEPSCs). ***B***, Example traces of LFP + whole-cell
1090 recording voltage-clamped at 0 mV to detect sIPSCs and swrIPSCs. ***C***, Diagram of LFP + whole-cell PC
1091 recording in 5xFAD/+;Thy1-GCaMP6f and Thy1-GCaMP6f littermate controls. ***D***, The frequency,
1092 amplitude, and normalized charge (integrated current per unit time) of sEPSCs did not differ between
1093 genotype (n_{cell} = 19 CT, 14 5xFAD; Frequency: $t_{(31)} = 0.706$, $p = 0.486$; Amplitude: $t_{(31)} = 1.286$, $p = 0.208$;
1094 Charge: $t_{(31)} = 0.961$, $p = 0.343$; unpaired t-tests). ***E***, Example of swrEPSCs. Both LFP and intracellular
1095 traces were filtered in the gamma (20-50 Hz) and ripple (120-220 Hz) ranges to cross-correlate. ***F***, The
1096 total excitatory charge during SWRs (swrEPSQ) was increased in 5xFAD mice ($t_{(31)} = 2.849$, $p = 0.0077$;
1097 unpaired t-test). ***G***, Cross-correlation of gamma (*left*) and ripple (*right*) between LFP and swrEPSCs. For
1098 both genotypes, the gamma and ripple band of swrEPSCs were significantly anti-correlated with the LFP
1099 (Gamma CT: $t_{(18)} = 7.393$, $p = 7.4 \times 10^{-7}$; Gamma 5xFAD: $t_{(13)} = 7.225$, $p = 6.7 \times 10^{-6}$; Ripple CT: $t_{(18)}$ =
1100 5.249, $p = 5.4 \times 10^{-5}$; Ripple 5xFAD: $t_{(13)} = 5.504$, $p = 0.0001$; 1-sample t-tests). In addition, the strength
1101 of anti-correlation was increased in 5xFAD mice for both gamma ($t_{(31)} = 2.363$, $p = 0.025$; unpaired t-test)
1102 and ripple ($t_{(31)} = 2.064$, $p = 0.047$, unpaired t-test). ***H-K*** same as ***D-G*** for IPSCs. ***H***, In 5xFAD mice,
1103 sIPSC frequency was decreased (n_{cell} = 21 CT, 16 5xFAD; $t_{(35)} = 2.276$, $p = 0.0291$; unpaired t-test), the
1104 amplitude was unchanged ($t_{(35)} = 1.514$, $p = 0.139$, unpaired t-test), and the normalized charge decreased
1105 ($t_{(35)} = 2.515$, $p = 0.0166$; unpaired t-test). ***I***, Example of swrIPSCs. ***J***, Inhibitory charge during SWRs
1106 (swrIPSQ) did not differ between genotype ($t_{(35)} = 1.328$, $p = 0.1928$, unpaired t-test). ***K***, The cross-
1107 correlations of LFP and swrIPSCs in the gamma and ripple bands were significantly correlated for both
1108 genotypes (Gamma CT: $t_{(20)} = 9.221$, $p = 1.2 \times 10^{-8}$; Gamma 5xFAD: $t_{(15)} = 13.36$, $p = 9.8 \times 10^{-10}$; Ripple
1109 CT: $t_{(20)} = 6.823$, $p = 1.2 \times 10^{-6}$; Ripple 5xFAD: $t_{(15)} = 6.777$, $p = 6.2 \times 10^{-6}$; 1-sample t-tests). Unlike for
1110 swrEPSCs, the strength of correlation was no different between genotype (Gamma: $t_{(35)} = 1.125$, p =
1111 0.268; Ripple: $t_{(35)} = 1.938$, $p = 0.0607$; unpaired t-tests). ***L***, Spontaneous synaptic E/I ratio of normalized
1112 charge for each cell (sEPSQ/sIPSQ). Spontaneous E/I ratio was significantly increased, driven by a
1113 decrease in inhibition (n_{cell} = 17 CT, 14 5xFAD; $t_{(29)} = 2.972$, $p = 0.0059$; unpaired t-test). ***M***, Synaptic E/I

1114 ratio for 100 ms window centered around SWR peak (swrEPSQ/swrIPSQ). As with spontaneous charge,
1115 the SWR E/I ratio was significantly increased ($t_{(29)} = 2.086$, $p = 0.0459$; unpaired t-test), however it was
1116 driven by an increase in excitation rather than a decrease in inhibition. ***N***, For both EPSCs and IPSCs
1117 during SWRs, the charge for each cell (EPSQ and IPSQ) was calculated in 2 ms bins by integrating the
1118 current in a 100 ms window centered around that bin. The dark lines represent the average charge across
1119 all cells, while the shaded region represents the SEM. ***F*** and ***J*** thus represent these curves at the y-
1120 intercept. For excitatory charge, there was a significant effect of genotype ($F_{(1,3100)} = 488.4$, $p < 10^{-15}$; 2-
1121 way ANOVA), as well as an interaction of genotype × bin ($F_{(99,3100)} = 2.820$, $p < 10^{-15}$). Asterisks indicate
1122 regions that survived Šidák's multiple comparisons * < 0.05, ** < 0.01. There was also a significant effect
1123 of genotype for inhibitory charge ($F_{(1,3500)} = 126.8$, $p < 10^{-15}$; 2-way ANOVA), however no bins survived
1124 multiple comparisons. ***O,*** the ratio of curves in ***N*** yields the synaptic E/I ratio during SWRs. There was a
1125 significant effect of genotype ($F_{(1,3100)} = 146.4$, $p < 10^{-15}$; 2-way ANOVA). *** < 0.001 indicates region that
1126 survived multiple comparisons. ***M*** represents these curves at the y-intercept. For all plots, individual data
1127 points represent a cell. Closed circles represent cells from males, open circles females. Bar plots
1128 represent normal data with Mean ± SEM. p-values indicated above brackets.
1129

1130 **Figure 6**: ***PV cells in CA1 delineate into basket (PVBCs), bistratified (PVBSCs), and axo-axonic***
1131 ***(PVAACs) cells. A***, Diagram of LFP + PV cell recording in 3 mo 5xFAD/+; PV^{Cre}/+;tdTom/+ and
1132 PV^{Cre}/+;tdTom/+ littermate controls. ***B***, Diagram of PV cell subtypes and their axonal targets in CA1 *str.*
1133 *pyr.* Examples of ***C.1***, PVBCs, ***C.2***, PVBSCs, and ***C.3***, PVAACs. Green fluorescence indicates avidin-
1134 fluorescein bound to the biocyin in the filled PV cell. Red fluorescence indicates PV^{Cre}/+;tdTom/+
1135 expression. Dashed grey lines approximately distinguish layers of hippocampus, *str. l.m. = stratum*
1136 *lacunosum-moleculare*, *str. rad. = stratum radiatum*, *str. pyr. = stratum pyramidale, str. or. = stratum*
1137 *oriens*. Notice that *str. pyr.* is dimly red due to the expression of other non-filled PVBCs targeting
1138 perisomatic regions of PCs. Scale bars = 100 µm. *Bottom traces*, Examples of LFP and cell-attached
1139 recording of spikes, which was used to aid in distinguishing PVBCs and PVAACs. PVAACs are unique
1140 in that they reduce their firing during SWRs. ***C.4***, Ankyrin G immunostaining showing co-localization of
1141 synaptic boutons with AIS of PCs for identified PVAAC. Scale bar = 10 µm. ***D***, Proportions of sorted cells
1142 in each genotype. There was no significant difference in proportions between genotype ($\chi^2_{(2)} = 1.09$, $p =$
1143 0.580; χ^2 Test), nor was there a significant deviation from expected proportions of 60% PVBC, 25%
1144 PVBSC, and 15% PVAAC ($\chi^2_{(2)} = 0.754$, $p = 0.686$; χ^2 Test).

1145 **Figure 7**: ***PV basket cells have selectively reduced spiking***. Spiking data for ***A***, PVBCs, ***B***, PVBSCs,
1146 and ***B***, PVAACs. ***A.1***, Spike rate of PVBCs during spontaneous and SWR periods, with an effect of
1147 genotype (n_{cell} = 13 CT, 16 5xFAD; $F_{(1,27)}$ = 10.42, p = 0.0033; 2-way RM ANOVA, align-rank transformed),
1148 no difference in spontaneous spike rate, but a decreased SWR spike rate in 5xFAD mice (Spont: p =
1149 0.209, SWR: p = 0.044; Mann-Whitney *post hoc*, Šidák correction). PVBC spike rate increased during
1150 SWR periods, with an effect of period ($F_{(1,27)}$ = 179.4, p = 1.9×10^{-13}), and increases in both control and
1151 5xFAD mice (CT: p = 0.00049, 5xFAD: p = 0.00012; Wilcoxon *post hoc*, Šidák correction). Additionally,
1152 there was an interaction of genotype × period ($F_{(1,27)}$ = 16.76, p = 0.00034), indicating that PVBC
1153 modulation of spiking during SWRs differed between genotype. ***A.2***, PVBC peri-SWR spike probability,
1154 with an effect of genotype ($F_{(1,2700)}$ = 267.3, p < 10^{-15}; 2-way ANOVA), and interaction of genotype × bin
1155 ($F_{(99,2700)}$ = 1.446, p = 0.0030). Asterisks indicate regions surviving Šidák's multiple comparisons
1156 correction. * < 0.05, ** < 0.01, *** < 0.001. ***A.3***, PVBC burst rate had tendency for decrease (U = 60, p =
1157 0.056, Mann-Whitney). ***A.4***, *left*, The fraction of SWRs with one or more PVBC spike did not differ (U =
1158 72, p = 0.170, Mann-Whitney), but *right,* the fraction of SWRs with a PVBC burst was reduced (U = 53,
1159 p = 0.025, Mann-Whitney). ***A.5***, Example of LFP and PVBC cell-attached traces for CT (*left*) and 5xFAD
1160 (*right*). Spike and SWR events are color-coded as in Fig. 4B. ***A.6***, PVBC spikes were phase-locked in
1161 the gamma range in 5xFAD mice (Z = 7.944, p = 0.00012; Raleigh's test), though not for controls (Z =
1162 2.477, p = 0.082; Raleigh's test), and with no difference in median phase angle (P = 0.144, p = 0.705;
1163 Circular median test). ***A.7***, PVBCs were phase-locked in the ripple range for both genotypes (CT: Z =
1164 6.006, p = 0.0014; 5xFAD: Z = 9.35, p = 1.7×10^{-5}; Raleigh's tests), with no difference in mean phase
1165 angle ($F_{(1,27)}$ = 1.335, p = 0.258; Watson-Williams). ***B.1***, Spike rates for PVBSCs during spontaneous and
1166 SWR periods, with no effect of genotype (n_{cell} = 5 CT, 10 5xFAD; $F_{(1,13)}$ = 1.345, p = 0.267; 2-way RM
1167 ANOVA, align-rank transformed), and no genotype differences for either period (Spont: p = 0.980, SWR:
1168 p = 0.763; Mann-Whitney *post hoc*, Šidák correction). PVBSCs increased their spike rate during SWRs,
1169 with an effect of period ($F_{(1,13)}$ = 30.6, p = 9.7×10^{-5}), and increases in 5xFAD but not control mice (CT: p
1170 = 0.121, 5xFAD: p = 0.019; Wilcoxon *post hoc*, Šidák correction). There was no interaction of genotype
1171 × period ($F_{(1,13)}$ = 2.563, p = 0.133). ***B.2***, PVBSC peri-SWR spike probability, with an effect of genotype

1172 ($F_{(1,1300)}$ = 33.9, p = 7.3 × 10^{-9}; 2-way ANOVA), no interaction of genotype × bin ($F_{(1,1300)}$ = 33.9, p = 7.3 ×
1173 10^{-9}), and no bins surviving multiple comparisons. ***B.3***, Burst rate for PVBSCs was unchanged (U = 22.5,
1174 p = 0.793, Mann-Whitney). ***B.4***, In PVBSCs the fraction of SWRs with at least one spike and with a burst
1175 were both unchanged (U = 21, p = 0.655; U = 16.5, p = 0.323; Mann-Whitney). ***B.5***, Example LFP and
1176 PVBSC cell-attached traces for control (*left*) and 5xFAD (*right*). ***B.6***, PVBSC spikes were phase-locked
1177 in the gamma range in 5xFAD mice (Z = 3.543, p = 0.024; Raleigh's test), though not for controls (Z =
1178 1.566, p = 0.216; Raleigh's test), and with no difference in median phase angle (P = 0.311, p = 0.577;
1179 Circular median test). ***B.7***, PVBSCs were not phase-locked in the ripple range (CT: Z = 1.631, p = 0.202;
1180 5xFAD: Z = 1.334, p = 0.270; Raleigh's tests). ***C.1***, Spike rates for PVAACs during spontaneous and
1181 SWR periods, with no effect of genotype (n_{cell} = 6 CT, 6 5xFAD; $F_{(1,10)}$ = 3.832, p = 0.079; 2-way RM
1182 ANOVA, align-rank transformed), and no genotype differences for either period (Spont: p = 0.909, SWR:
1183 p = 0.178; Mann-Whitney *post hoc*, Šidák correction). While PVAACs did see an effect of period ($F_{(1,10)}$ =
1184 16.67, p = 0.0022), neither in control nor 5xFAD mice was the increase significant (CT: p = 0.527, 5xFAD:
1185 p = 0.062; Wilcoxon *post hoc*, Šidák correction), nor was there an interaction of genotype × period ($F_{(1,10)}$
1186 = 3.208, p = 0.104). ***C.2***, PVAAC peri-SWR spike probability, with an effect of genotype ($F_{(1,1000)}$ = 30.15,
1187 p = 5.1 × 10^{-8}; 2-way ANOVA), no interaction of genotype × bin ($F_{(99,1000)}$ = 0.339, p > 0.999), and no bins
1188 surviving multiple comparisons. ***C.3***, Burst rate for PVAACs was unchanged (U = 24, p > 0.999, Mann-
1189 Whitney). ***C.4***, In PVAACs, the fraction of SWRs with at least one spike and with a burst were both
1190 unchanged (U = 6, p = 0.065; U = 10.5, p = 0.182; Mann-Whitney). ***C.5***, Example LFP and PVAAC cell-
1191 attached traces for CT (*left*) and 5xFAD (*right*). ***C.6***, PVAAC spikes were phase-locked in the gamma
1192 range in CT mice (Z = 4.427, p = 0.005; Raleigh's test), though not for 5xFAD mice (Z = 0.913, p = 0.421;
1193 Raleigh's test), and with a tendency for a difference in median phase angle (P = 3.600, p = 0.058; Circular
1194 median test). ***C.7***, PVAACs were phase-locked in the ripple range for both genotype (CT: Z = 3.749, p =
1195 0.0015; 5xFAD: Z = 3.542, p = 0.0020; Raleigh's tests), with a difference in mean phase angle ($F_{(1,9)}$ =
1196 5.677, p = 0.044; Watson-Williams). For all plots, individual data points represent a cell. Closed circles
1197 represent cells from males, open circles females. Box-whisker plots represent non-normal data with
1198 Median and IQRs. p-values indicated above brackets.

1199 **Figure 8**: ***PV basket cells have selective decrease in excitatory synaptic input and decreased E/I***
1200 ***ratio***. ***A***, Diagram of LFP + whole-cell PV cell recording in 3 mo 5xFAD/+; PV^{Cre}/+;tdTom/+ and
1201 PV^{Cre}/+;tdTom/+ littermate controls. ***B-D***, Example recordings of excitatory synaptic input during
1202 spontaneous and SWR periods in ***B.1***, PVBCs, ***C.1***, PCBSCs, and ***C.1***, PVAACs, voltage-clamped at -
1203 70 mV. ***E.1***, Inhibitory synaptic currents voltage-clamped at 0 mV in a subset of PVBCs. ***B.2***, sEPSCs
1204 were unchanged in PVBCs (n_{cell} = 12 CT, 16 5xFAD; Frequency: $t_{(26)}$ = 1.298, p = 0.2056; Amplitude: $t_{(26)}$
1205 = 0.5448, p = 0.5906; unpaired t-tests). ***B.3***, In PVBCs, the excitatory charge in a 100 ms window
1206 centered around the SWR peak (swrEPSQ) was significantly reduced ($t_{(26)}$ = 3.196, p = 0.0036, unpaired
1207 t-test). ***C.2-3***, In PVBSCs, sEPSCs and swrEPSQ were unchanged (n_{cell} = 4 CT, 6 5xFAD; Frequency:
1208 $t_{(8)}$ = 0.9898, p = 0.3513; Amplitude: $t_{(8)}$ = 0.0576, p = 0.9555; swrEPSQ: $t_{(8)}$ = 0.9968, p = 0.3480; unpaired
1209 t-tests). ***D.2-3***, In PVAACs, sEPSCs and swrEPSQ were unchanged (n_{cell} = 5 CT, 6 5xFAD; Frequency:
1210 $t_{(9)}$ = 0.1289, p = 0.9003; Amplitude: $t_{(9)}$ = 2.112, p = 0.0639; swrEPSQ: $t_{(9)}$ = 1.625, p = 0.1385; unpaired
1211 t-tests). ***E.2-3***, In PVBCs at 0 mV, sIPSCs are swrIPSQ were unchanged (n_{cell} = 8 CT, 8 5xFAD;
1212 Frequency: $t_{(14)}$ = 0.4477, p = 0.6612; Amplitude: $t_{(14)}$ = 3390, p = 0.7396; swrIPSQ: $t_{(14)}$ = 0.00832, p =
1213 0.9935; unpaired t-tests). ***F***, The running charge (EPSQ and IPSQ) in a 100 ms window for PVBCs. Dark
1214 lines represent the average charge across all cells, shaded region represents the SEM, y-axis represents
1215 SWR peak. For EPSQ, there was a significant effect of genotype ($F_{(1,2500)}$ = 664.2, p < 10^{-15}; 2-way
1216 ANOVA), as well as an interaction of genotype × bin ($F_{(99,2500)}$ = 2.211, p = 1.9 × 10^{-10}). Asterisks indicate
1217 regions that survived Šidák's multiple comparisons * < 0.05, ** < 0.01, *** < 0.01. There was no effect of
1218 genotype for IPSQ ($F_{(1,1400)}$ = 2.123, p = 0.1453, 2-way ANOVA). ***G,*** the ratio of curves in ***F*** gives the
1219 synaptic E/I ratio during SWRs, with a significant effect of genotype ($F_{(1,1300)}$ = 338.7, p < 10^{-15}, 2-way
1220 ANOVA). ** < 0.01 indicates region that survived multiple comparisons. ***H***, There was no change in
1221 spontaneous E/I ratio (ratio of normalized charge (integrated current / unit time)) for PVBCs ($t_{(14)}$ = 0.929,
1222 p = 0.368, unpaired t-test). However, the SWR E/I ratio was significantly decreased ($t_{(14)}$ = 2.701, p =
1223 0.017, unpaired t-test). ***I***, Linear regression of spike rate during SWRs vs the E/I ratio. For PVBCs from
1224 CT mice, there was a non-zero slope, indicating a positive correlation (n_{cell} = 8, R^2 = 0.6245, $F_{(1,6)}$ = 9.977,
1225 p = 0.020, Linear Regression), however there was no correlation for cells from 5xFAD mice (n_{cell} = 8, R^2

1226 = 0.0092, $F_{(1,6)}$ = 0.0555, p = 0.822). For all plots, individual data points represent a cell. Closed circles
1227 represent cells from males, open circles females. Bar plots represent normal data with Mean ± SEM. p-
1228 values indicated above brackets.

	Electrophysiology + Imaging (Fig. 2-8)				Behavior (Fig. 1)			
	Control 1mo	*5xFAD 1mo*	***Control 3mo***	***5xFAD 3mo***	*Control 1mo*	*5xFAD 1mo*	*Control 3mo*	*5xFAD 3mo*
n_{mice}	10 (6f)	10 (4f)	27 (17f)	29 (12f)	10 (2f)	10 (6f)	15 (7f)	12 (8f)
Age (postnatal days)	40.2 ± 4.4 (34-46)	40.4 ± 4.6 (34-46)	95.8 ± 6.0 (83-105)	94.5 ± 5.8 (85-105)	42.0 ± 5.2 (36-47)	43.8 ± 4.2 (36-47)	91.8 ± 5.2 (87-99)	92.5 ± 5.4 (87-99)
n_{slice} *(range 2 - 8)*	5.6 ± 0.8	4.0 ± 1.8	3.9 ± 1.3	3.2 ± 1.4				
% slices with SWRs	93.8 ± 8.1%	70.8 ± 22.0%	72.4 ± 19.8%	66.3 ± 26.1%				

	Thy1-GCaMP6f (Fig. 3-5)		PV^{Cre}/+;tdTom/+ (Fig. 6-8)		Thy1-GCaMP6f;PV^{Cre}/+;tdTom/+ (Fig. 4-8)	
	Control	*5xFAD*	*Control*	*5xFAD*	*Control*	*5xFAD*
n_{mice}	10 (5f)	11 (5f)	13 (8f)	11 (5f)	4 (4f)	7 (2f)
Age (postnatal days)	95.0 ± 7.4 (83-105)	93.4 ± 3.2 (85-102)	96.8 ± 5.7 (88-104)	97.4 ± 6.0 (88-105)	94.8 ± 3.2 (90-97)	91.6 ± 2.1 (90-95)
n_{slice} *(range 2 - 8)*	3.9 ± 1.1	2.8 ± 1.3	3.8 ± 1.5	4.9 ± 2.1	4.5 ± 1.3	3.6 ± 1.8
% slices with SWRs	75.5 ± 20.2%	67.9 ± 26.2%	67.4 ± 20.5%	68.2 ± 25.3%	80.8 ± 16.4%	60.7 ± 30.5%
$n_{cell\text{-}attached}$	41 (PC)	46 (PC)	54 (PV)	37 (PV)	19 (PV)	9 (PC); 19 (PV)
$n_{whole\text{-}cell}$	19 (PC)	13 (PC)	11 (PV)	16 (PV)	10 (PV)	1 (PC); 13 (PV)

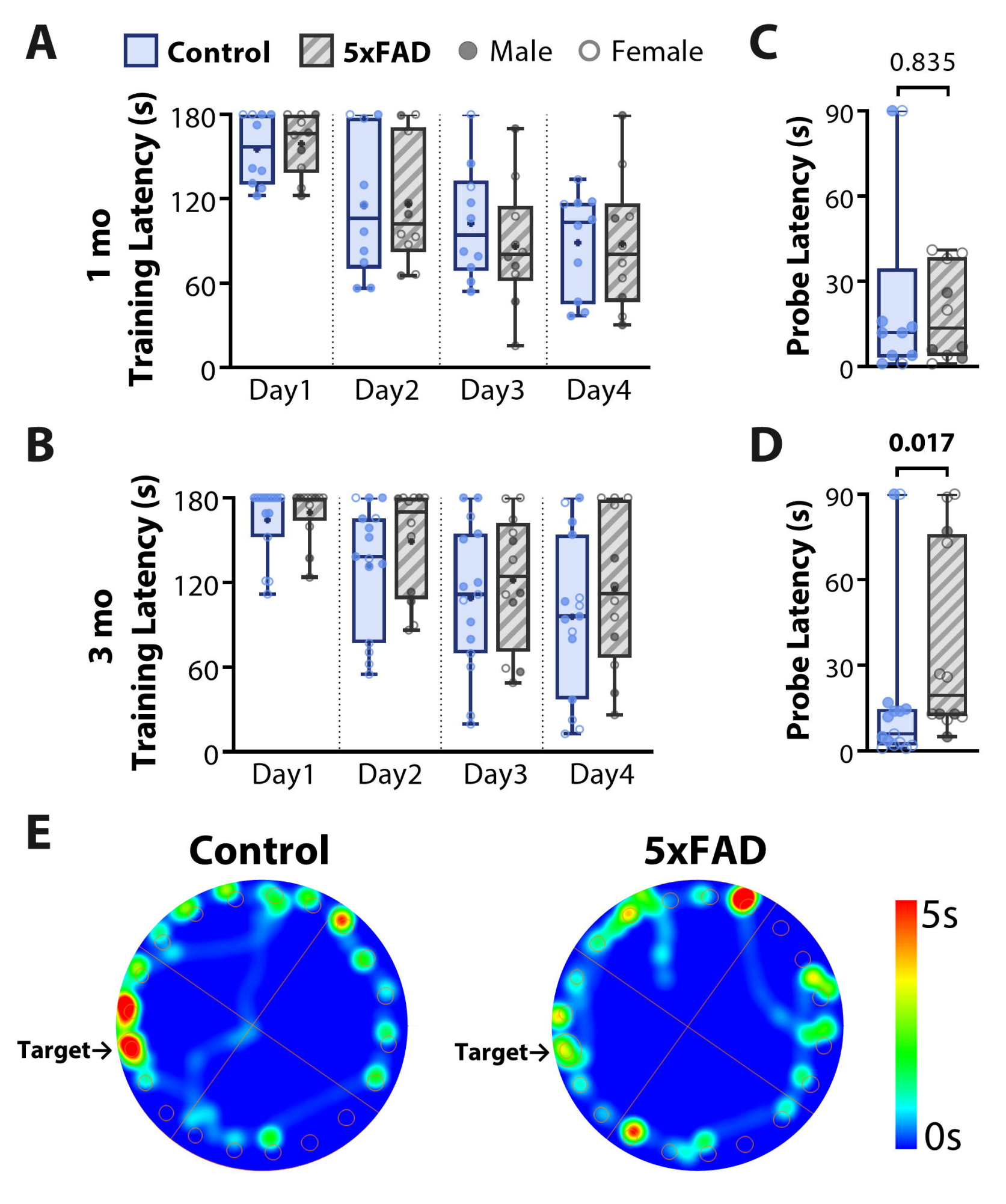
A
Control
5xFAD
Male
Female
1 mo
Training Latency (s)
180
120
60
0
Day1
Day2
Day3
Day4
C
0.835
Probe Latency (s)
90
60
30
0
B
3 mo
Training Latency (s)
180
120
60
0
Day1
Day2
Day3
Day4
D
0.017
Probe Latency (s)
90
60
30
0
E
Control
5xFAD
Target→
Target→
5s
0s

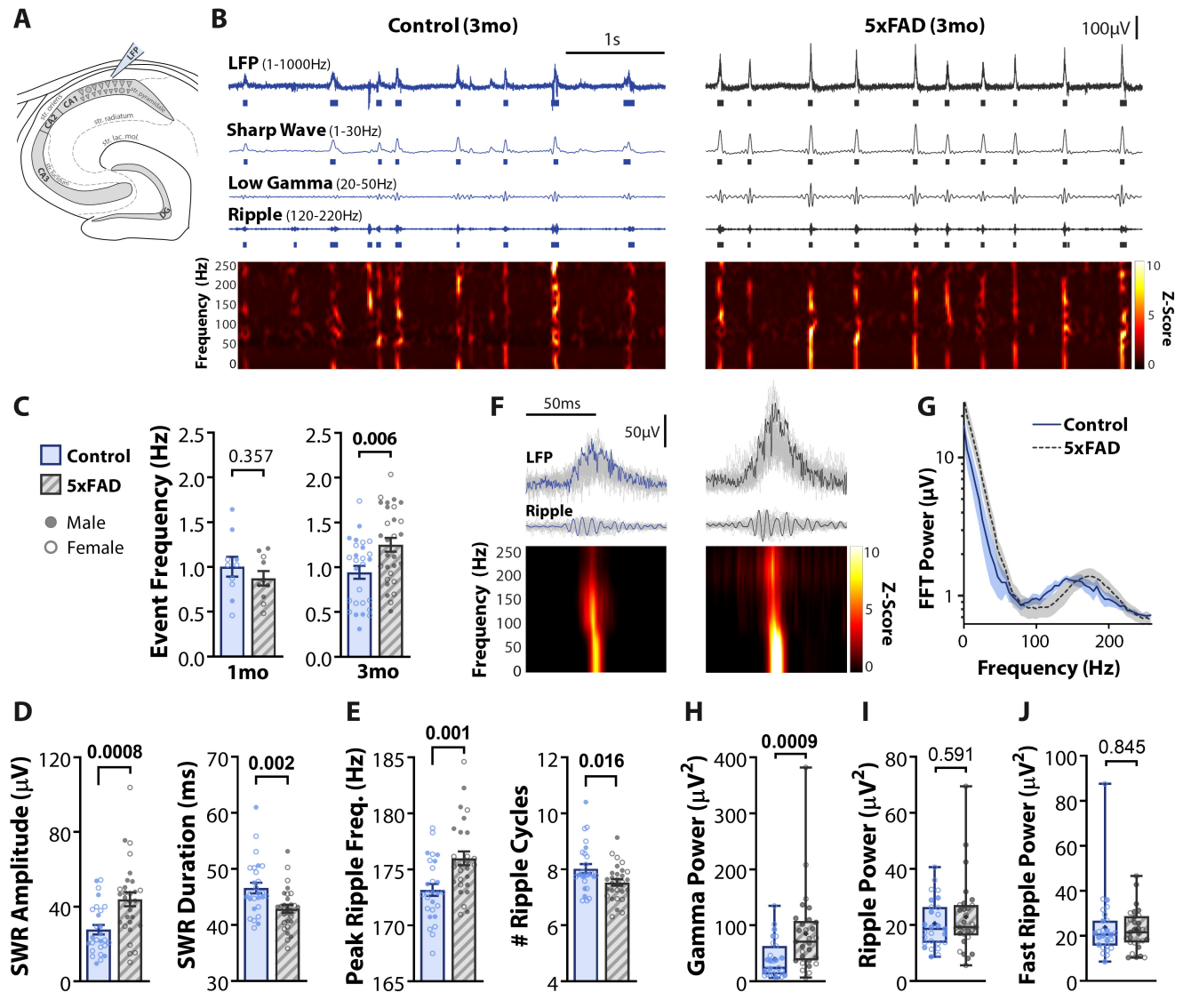
A
LFP
CA1
CA3
DG
str. pyramidale
str. radiatum
str. lac. mol.
B
Control (3mo)
5xFAD (3mo)
1s
100µV
LFP (1-1000Hz)
Sharp Wave (1-30Hz)
Low Gamma (20-50Hz)
Ripple (120-220Hz)
Frequency (Hz)
Z-Score
C
Control
5xFAD
Male
Female
Event Frequency (Hz)
0.357
0.006
1mo
3mo
F
50ms
50µV
LFP
Ripple
Frequency (Hz)
Z-Score
G
Control
5xFAD
FFT Power (µV)
Frequency (Hz)
D
SWR Amplitude (µV)
0.0008
SWR Duration (ms)
0.002
E
Peak Ripple Freq. (Hz)
0.001
Ripple Cycles
0.016
H
Gamma Power (µV²)
0.0009
I
Ripple Power (µV²)
0.591
J
Fast Ripple Power (µV²)
0.845

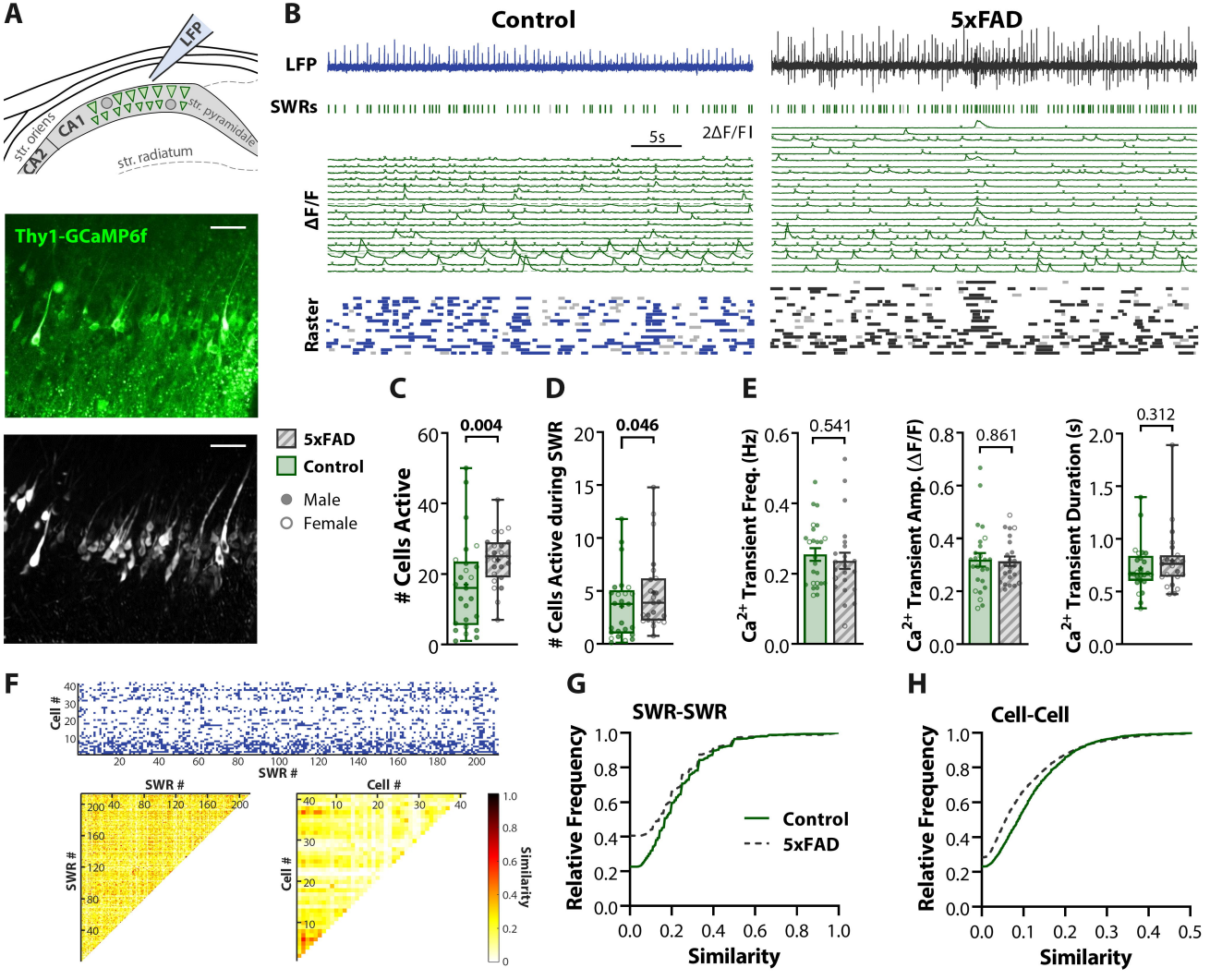
A
LFP
str. oriens
CA2
CA1
str. pyramidale
str. radiatum
Thy1-GCaMP6f
B
Control
5xFAD
LFP
SWRs
5s
2ΔF/F
ΔF/F
Raster
5xFAD
Control
Male
Female
C
Cells Active
0.004
D
Cells Active during SWR
0.046
E
Ca2+ Transient Freq. (Hz)
0.541
Ca2+ Transient Amp. (ΔF/F)
0.861
Ca2+ Transient Duration (s)
0.312
F
Cell #
SWR #
SWR #
Cell #
Similarity
G
SWR-SWR
Relative Frequency
Control
5xFAD
Similarity
H
Cell-Cell
Relative Frequency
Similarity

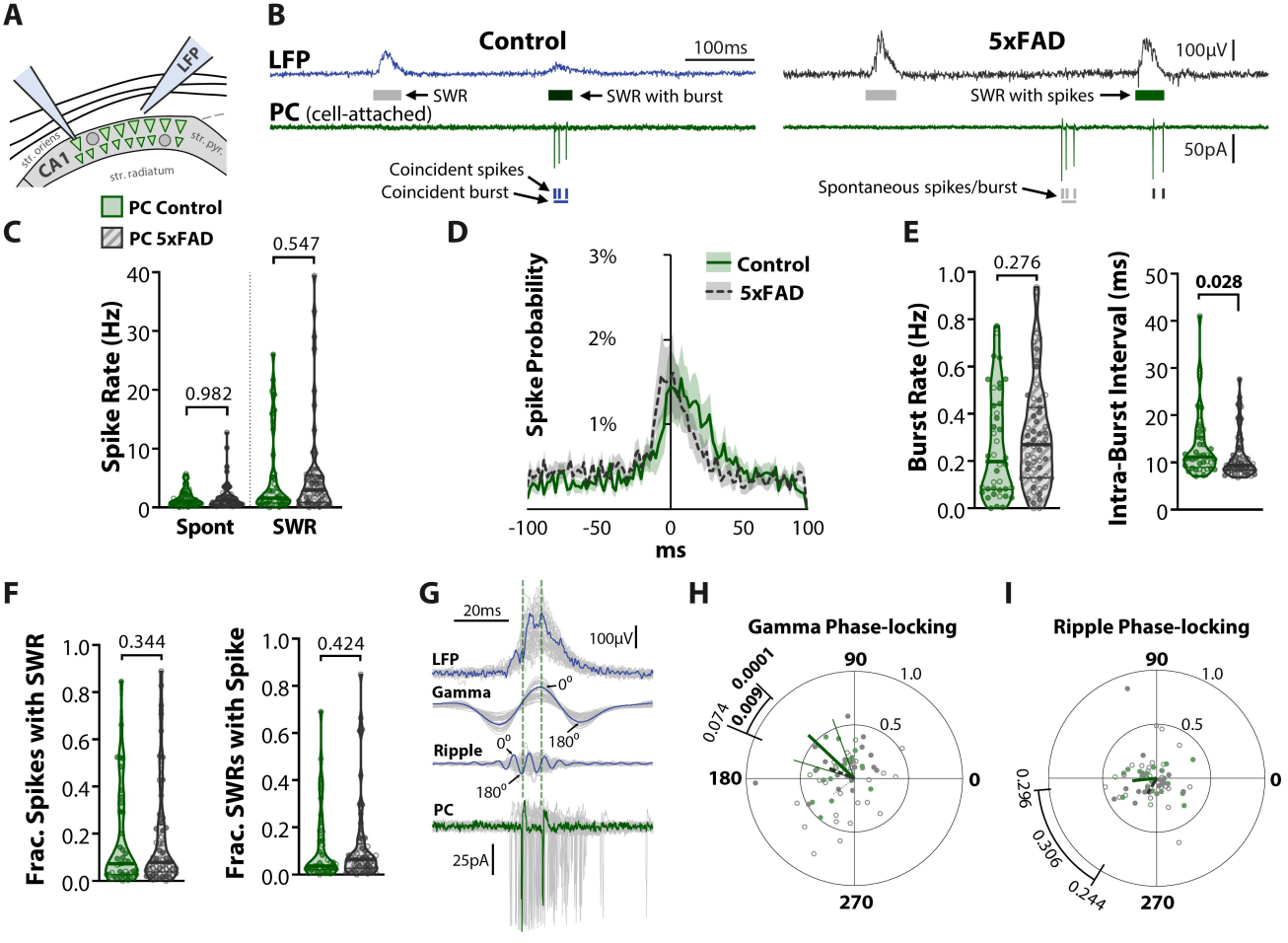
A
LFP
CA1
str. oriens
str. pyr.
str. radiatum
PC Control
PC 5xFAD
B
Control
LFP
100ms
SWR
SWR with burst
PC (cell-attached)
Coincident spikes
Coincident burst
5xFAD
100µV
SWR with spikes
50pA
Spontaneous spikes/burst
C
Spike Rate (Hz)
0.982
0.547
Spont
SWR
D
Spike Probability
3%
2%
1%
Control
5xFAD
-100
-50
0
50
100
ms
E
Burst Rate (Hz)
0.276
Intra-Burst Interval (ms)
0.028
F
Frac. Spikes with SWR
0.344
Frac. SWRs with Spike
0.424
G
20ms
100µV
LFP
Gamma
0°
Ripple
0°
180°
180°
PC
25pA
H
Gamma Phase-locking
90
180
0
270
1.0
0.5
0.0001
0.009
0.074
I
Ripple Phase-locking
90
180
0
270
1.0
0.5
0.296
0.306
0.244

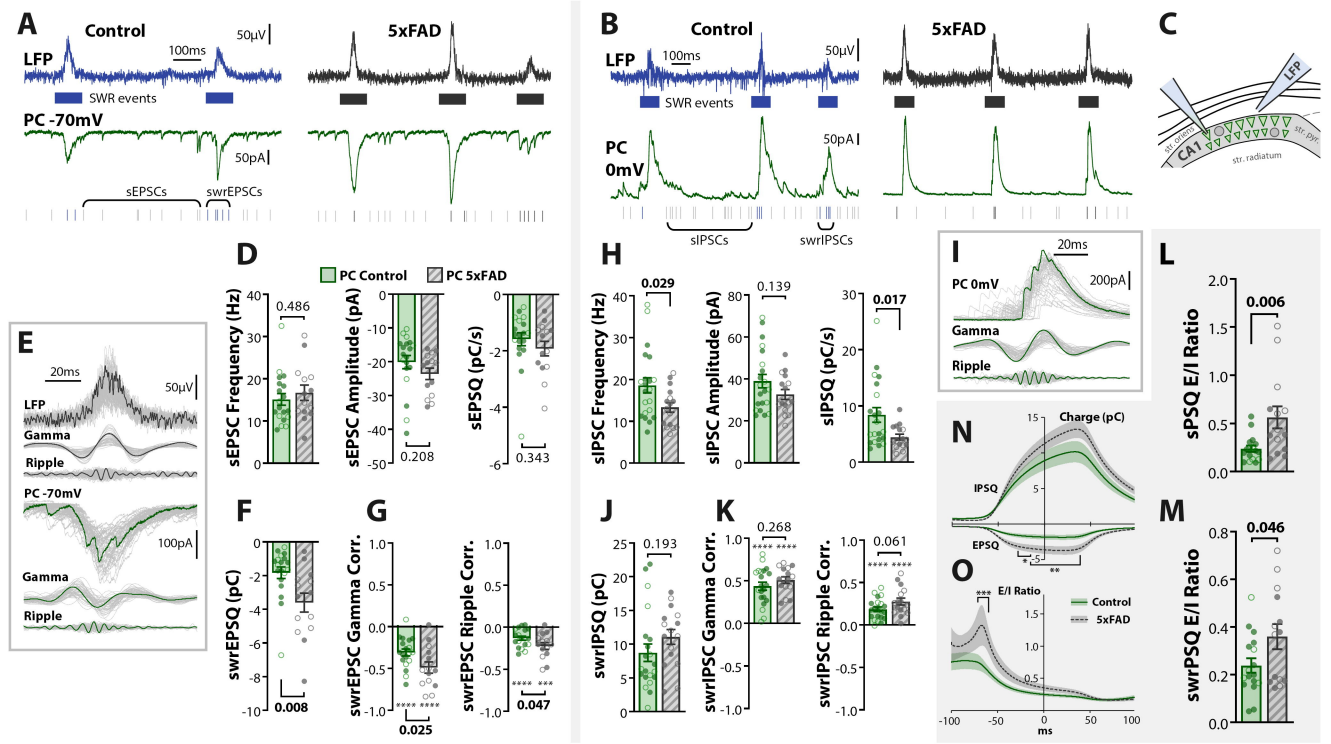
A
Control
5xFAD
LFP
100ms
50µV
SWR events
PC -70mV
50pA
sEPSCs
swrEPSCs
B
Control
5xFAD
LFP
100ms
50µV
SWR events
PC 0mV
50pA
sIPSCs
swrIPSCs
C
LFP
str. oriens
CA1
str. pyr.
str. radiatum
D
PC Control
PC 5xFAD
sEPSC Frequency (Hz)
0.486
sEPSC Amplitude (pA)
0.208
sEPSQ (pC/s)
0.343
E
20ms
50µV
LFP
Gamma
Ripple
PC -70mV
100pA
Gamma
Ripple
F
swrEPSQ (pC)
0.008
G
swrEPSC Gamma Corr.
0.025
swrEPSC Ripple Corr.
0.047
H
sIPSC Frequency (Hz)
0.029
sIPSC Amplitude (pA)
0.139
sIPSQ (pC/s)
0.017
I
20ms
PC 0mV
200pA
Gamma
Ripple
J
swrIPSQ (pC)
0.193
K
swrIPSC Gamma Corr.
0.268
swrIPSC Ripple Corr.
0.061
L
sPSQ E/I Ratio
0.006
N
Charge (pC)
IPSQ
EPSQ
O
E/I Ratio
Control
5xFAD
ms
M
swrPSQ E/I Ratio
0.046

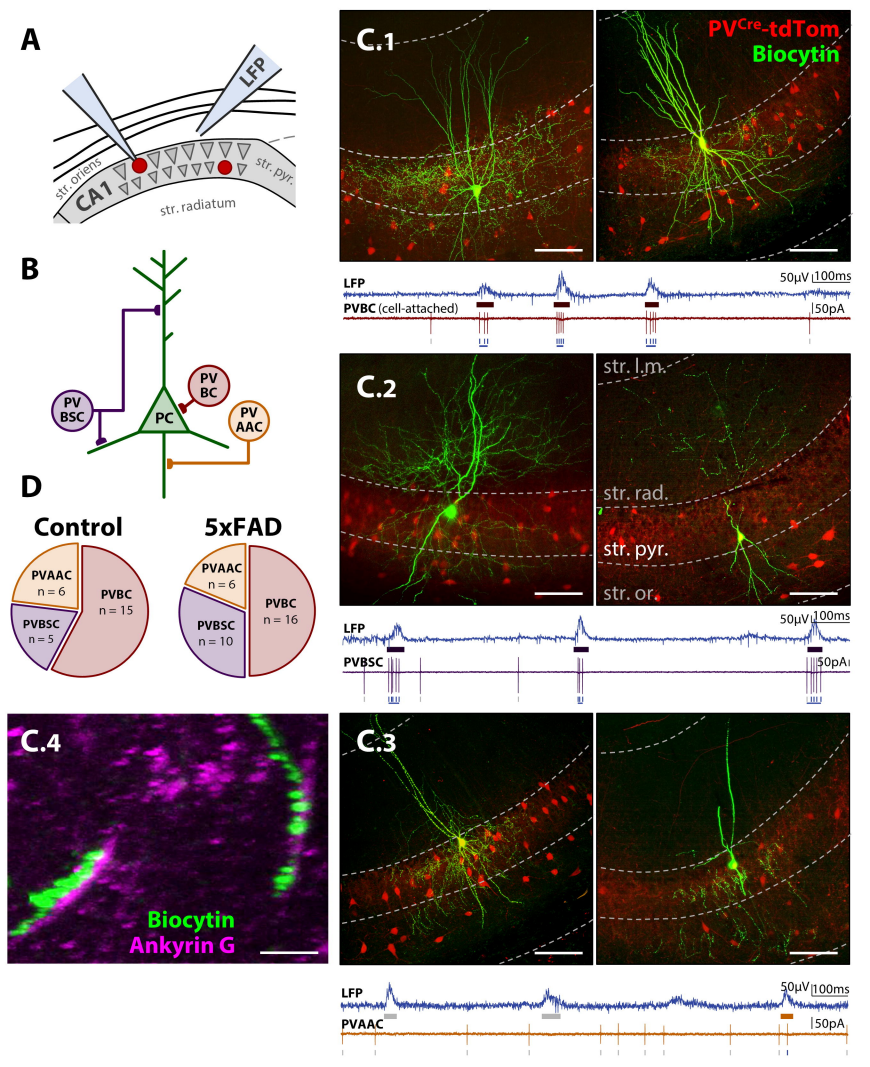
A
LFP
str. oriens
CA1
str. pyr.
str. radiatum
B
PV BSC
PC
PV BC
PV AAC
D
Control
PVAAC n = 6
PVBC n = 15
PVBSC n = 5
5xFAD
PVAAC n = 6
PVBC n = 16
PVBSC n = 10
C.1
PVCre-tdTom
Biocytin
LFP
50µV
100ms
PVBC (cell-attached)
50pA
C.2
str. l.m.
str. rad.
str. pyr.
str. or.
LFP
50µV
100ms
PVBSC
50pA
C.4
Biocytin
Ankyrin G
C.3
LFP
50µV
100ms
PVAAC
50pA

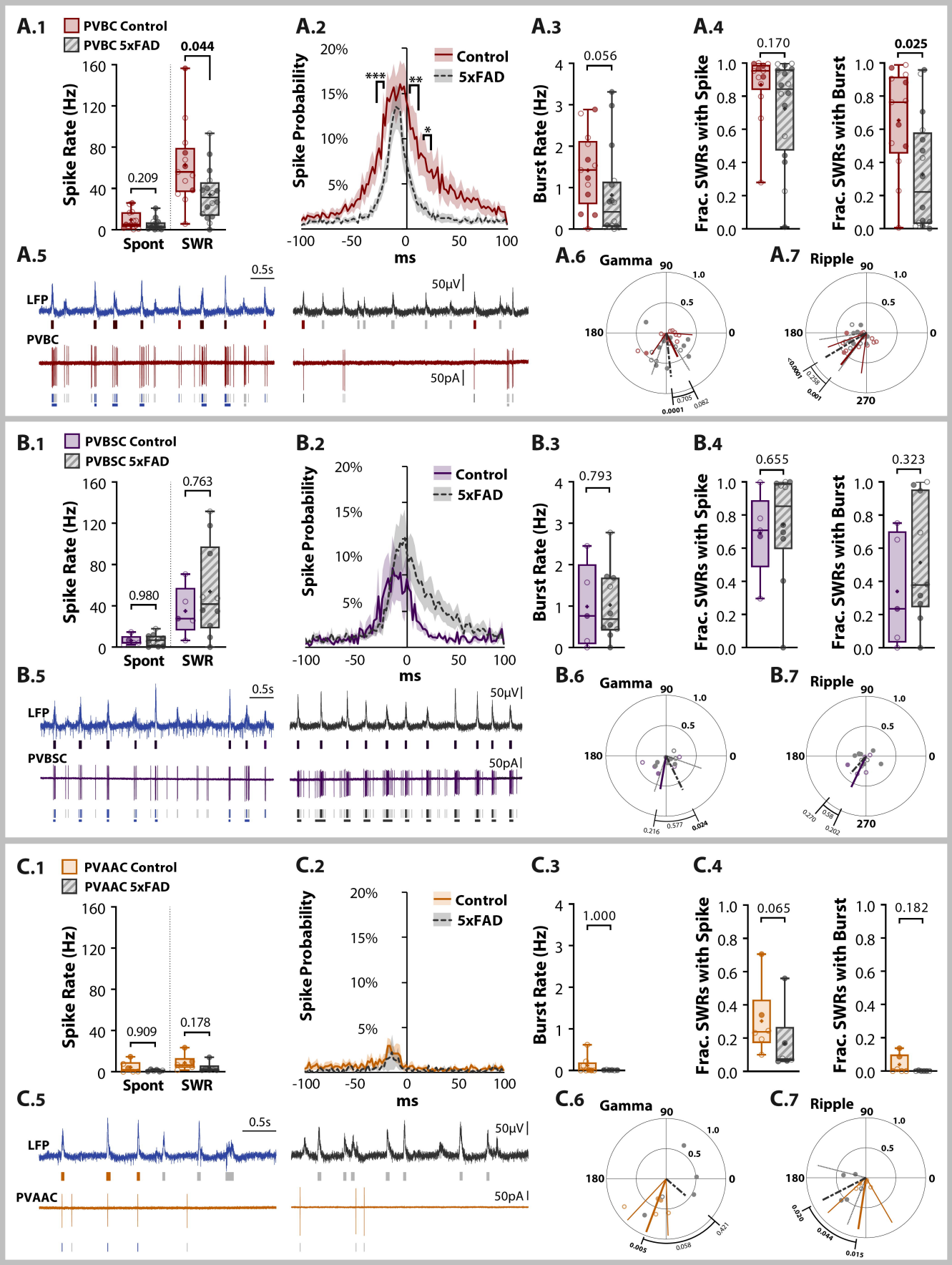
A.1
PVBC Control
PVBC 5xFAD
Spike Rate (Hz)
0.209
0.044
Spont
SWR
A.2
Control
5xFAD
Spike Probability
***
**
*
ms
A.3
Burst Rate (Hz)
0.056
A.4
Frac. SWRs with Spike
0.170
Frac. SWRs with Burst
0.025
A.5
0.5s
LFP
PVBC
50µV
50pA
A.6
Gamma
A.7
Ripple
B.1
PVBSC Control
PVBSC 5xFAD
0.980
0.763
B.2
B.3
0.793
B.4
0.655
0.323
B.5
PVBSC
B.6
B.7
C.1
PVAAC Control
PVAAC 5xFAD
0.909
0.178
C.2
C.3
1.000
C.4
0.065
0.182
C.5
PVAAC
C.6
C.7

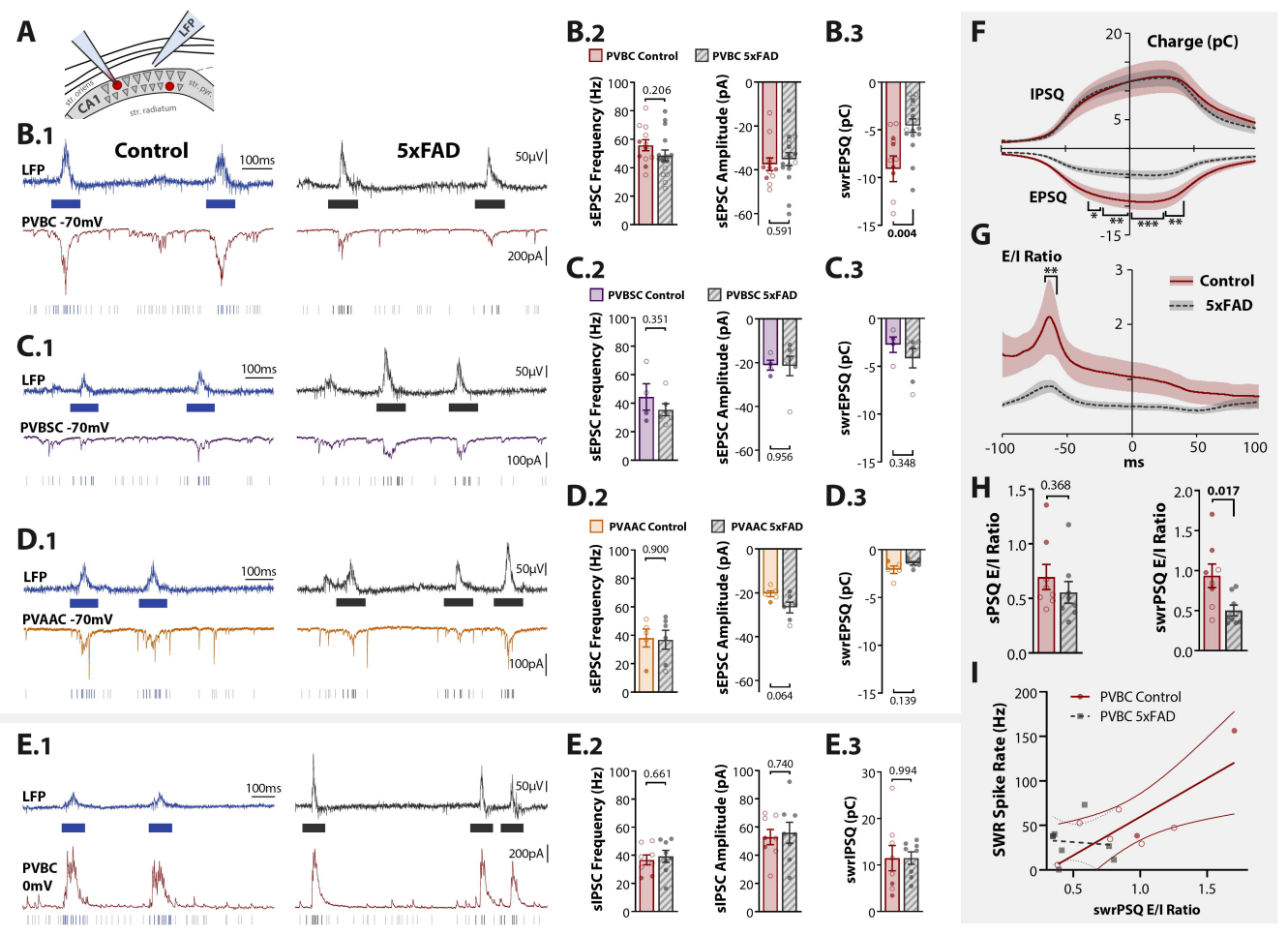
A
LFP
CA1
str. oriens
str. pyr.
str. radiatum
B.1
Control
5xFAD
LFP
PVBC -70mV
100ms
50µV
200pA
C.1
PVBSC -70mV
100pA
D.1
PVAAC -70mV
E.1
PVBC 0mV
B.2
PVBC Control
PVBC 5xFAD
sEPSC Frequency (Hz)
0.206
B.3
sEPSC Amplitude (pA)
0.591
swrEPSQ (pC)
0.004
C.2
PVBSC Control
PVBSC 5xFAD
0.351
C.3
0.956
0.348
D.2
PVAAC Control
PVAAC 5xFAD
0.900
D.3
0.064
0.139
E.2
sIPSC Frequency (Hz)
0.661
E.3
sIPSC Amplitude (pA)
0.740
swrIPSQ (pC)
0.994
F
Charge (pC)
IPSQ
EPSQ
G
E/I Ratio
Control
5xFAD
ms
H
sPSQ E/I Ratio
0.368
swrPSQ E/I Ratio
0.017
I
PVBC Control
PVBC 5xFAD
SWR Spike Rate (Hz)
swrPSQ E/I Ratio